Bioactive Materials 25 (2023) 223–238

Contents lists available at ScienceDirect

Bioactive Materials

journal homepage: www.keaipublishing.com/en/journals/bioactive-materials

A "built-up" composite film with synergistic functionalities on Mg–2Zn–1Mn bioresorbable stents improves corrosion control effects and biocompatibility

Zhenglong Dou [a], Shuiling Chen [a], Jiacheng Wang [a], Li Xia [a], Manfred F. Maitz [a,e], Qiufen Tu [a], Wentai Zhang [b], Zhilu Yang [b,c,d,**], Nan Huang [a,b,*]

[a] Key Lab of Advanced Technology of Materials of Education Ministry, School of Materials Science and Engineering, Southwest Jiaotong University, Chengdu, 610031, China
[b] Affiliated Dongguan Hospital, Southern Medical University, Dongguan, Guangdong, 523059, China
[c] Guangdong Provincial Key Laboratory of Cardiac Function and Microcirculation, Guangzhou, Guangdong, 510080, China
[d] Department of Cardiology, Third People's Hospital of Chengdu Affiliated to Southwest Jiaotong University, Chengdu, 610031, China
[e] Max Bergmann Center of Biomaterials Dresden, Leibniz Institute of Polymer Research Dresden, Hohe Strasse 6, 01069, Dresden, Germany

ARTICLE INFO

Keywords:
Magnesium alloys
Bioresorbable stents
Composite coating
Corrosion control
Biocompatibility

ABSTRACT

Control of premature corrosion of magnesium (Mg) alloy bioresorbable stents (BRS) is frequently achieved by the addition of rare earth elements. However, limited long-term experience with these elements causes concerns for clinical application and alternative methods of corrosion control are sought after. Herein, we report a "built-up" composite film consisting of a bottom layer of MgF_2 conversion coating, a sandwich layer of a poly (1, 3-trimethylene carbonate) (PTMC) and 3-aminopropyl triethoxysilane (APTES) co-spray coating (PA) and on top a layer of poly (lactic-co-glycolic acid) (PLGA) ultrasonic spray coating to decorate the rare earth element-free Mg–2Zn–1Mn (ZM21) BRS for tailoring both corrosion resistance and biological functions. The developed "built-up" composite film shows synergistic functionalities, allowing the compression and expansion of the coated ZM21 BRS on an angioplasty balloon without cracking or peeling. Of special importance is that the synergistic corrosion control effects of the "built-up" composite film allow for maintaining the mechanical integrity of stents for up to 3 months, where complete biodegradation and no foreign matter residue were observed about half a year after implantation in rabbit iliac arteries. Moreover, the functionalized ZM21 BRS accomplished re-endothelialization within one month.

1. Introduction

Mg alloy bioresorbable stents (BRS) are a promising alternative to permanent stents due to their absorbability and excellent biocompatibility [1,2]. However, one of the major factors that limit its clinical application is the intrinsic rapid degradation rate [3–5]. Many efforts have been made to improve Mg alloy corrosion resistance via material optimization and surface coatings.

Alloying and purification are the two major means of material optimization. Although purification may significantly improve the corrosion properties of Mg alloys, it weakens their mechanical properties [6,7]. Alloying adjusts the phase composition and distribution, prevents micro-couple corrosion, and forms a denser and more stable passivation film [8,9]. Aluminum (Al), zinc (Zn), manganese (Mn), calcium (Ca), lithium (Li), zirconium (Zr), strontium (Sr), and rare earth elements are the most commonly used elements for alloying Mg [10–12]. However, only a few alloying elements are suitable for degradable Mg alloys from a medical perspective [6,13]. Some studies have shown that the addition of rare earth elements can inhibit micro galvanic corrosion of Mg alloys [14]. However, the biocompatibility of rare earth elements remains controversial [15,16]. Zn is a vital element in the human body; the addition of Zn to Mg significantly enhanced its corrosion resistance along with a slight improvement of its mechanical properties [17]. Mn can also eliminate impurities like Fe in Mg alloys

Peer review under responsibility of KeAi Communications Co., Ltd.
* Corresponding author. Affiliated Dongguan Hospital, Southern Medical University, Dongguan, Guangdong, 523059, China.
** Corresponding author. Affiliated Dongguan Hospital, Southern Medical University, Dongguan, Guangdong, 523059, China.
E-mail addresses: zhiluyang1029@smu.edu.cn (Z. Yang), huangnan1956@163.com (N. Huang).

https://doi.org/10.1016/j.bioactmat.2023.02.004
Received 7 November 2022; Received in revised form 4 February 2023; Accepted 4 February 2023

[18,19]. Although significant progress has been made in improving the corrosion resistance of Mg through alloying, its clinical application is still limited by its insufficient corrosion control effects *in vivo* [20].

Surface modification preserves key material properties while improving corrosion resistance and biocompatibility compared to alloying [21–24]. According to the different coating preparation methods, surface modification can be divided into chemical modification, physical modification, and composite modification [25–27]. Fluoridation treatment is one of the dominant chemical modifications of Mg alloys, being simple, effective and economical [26]. Furthermore, the formed MgF_2 layer is beneficial to the improvement of coating adhesion and corrosion resistance [28–31]. However, a single MgF_2 conversion coating is not appropriate for the final surface modification of Mg alloy stents because the coating is particularly brittle and easily cracks upon deformation [31].

In contrast, polymer coatings exhibit excellent ductility and still provide complete coverage of the substrate even when subjected to plastic deformation. Several polymer materials have been widely employed in the surface protection of Mg alloys, such as polylactic acid (PLA) [32–34], polycaprolactone (PCL) [32,35], poly (lactic-co-glycolic acid) (PLGA) [36,37], and a poly (1, 3-trimethylene carbonate) (PTMC) [38,39]. PLA and PCL's bulk erosion behavior [31] and their acidic degradation products [40] may accelerate Mg alloy corrosion [32].

PTMC has been demonstrated to degrade by surface erosion [41], which provides long-term effective corrosion protection for Mg alloys. More importantly, the hydrolysis of PTMC is an approximately net neutral ionic process, with a pH that remains within the physiological pH during degradation. This feature differs from others usually considered polymers for implant corrosion prevention [38]. The poor stiffness and high viscosity of PTMC remain barriers to its application in Mg alloy BRS. PLGA is an elastomeric copolymer approved by the FDA [42,43]. Previous research has revealed that PLGA has tremendous potential as a surface coating for Mg alloys due to its excellent biocompatibility, strong hydrophobicity, and drug-carrying ability [44–46].

Although reasonable surface treatment improves the corrosion resistance of Mg alloy BRS as compared to bare stents, the inadequate bonding force between the coating and the Mg alloy substrate and the accelerated corrosion of the stent caused by acidic corrosion products remain significant challenges for existing coating techniques. Accordingly, rare earth-free Mg alloy BRS with sufficient durability have not yet been accomplished, with the exception of Maris stents [47].

Here, we adopted the rare earth-free ZM21 alloy for the stent body and developed a "built-up" composite film based on biocompatibility and degradation considerations. The composite film is made up of a PTMC and APTES composite coating in the middle, a uniform and dense MgF_2 layer at the bottom, and a PLGA layer on top. Based on the inspiration of solid solution strengthening of alloys, a small amount of APTES was added as a strengthening phase in the PTMC coating by physical spraying. APTES has been confirmed to degrade into a single molecule of $Si(OH)_4$ and would be removed by the urinary system without adverse tissue reactions, and silane-based coatings have also been certified to have excellent biocompatibility [36,48,49]. The PA coating not only has a corrosion control effect on the substrate but also effectively blocks the weakly acidic corrosion products of PLGA degradation.

All of the corrosion samples in this study are based on stents to reflect the service conditions of the final device more accurately, and all stents have been compressed onto balloons and expanded before evaluation. *In vitro* immersion tests in simulated body solution (SBF) were used to assess the degradation properties of the composite-coated stents comprehensively, and the *in vivo* degradation behavior of the stents was evaluated by implantation experiments. The primary purpose of this study is to establish a complete corrosion evaluation mechanism and the corresponding relationship between *in vivo* and *in vitro* corrosion by evaluating the degradation performance of ZM21 BRS *in vivo* and *in vitro*, as well as to assess the biocompatibility of MgF_2-PA-PLGA stents.

2. Experimental methods

2.1. Materials

Coronary stents and metal sheets of the rare earth element-free ZM21 were provided by Baier Maidike Medical Technology Co., Ltd. (Chengdu, China). The actual chemical composition of ZM21 is listed in Table 1. PTMC (Mw = 200000) and PLGA (Mw = 100000, Mw = 500000, Mw = 800000, with a GA:LA ratio of 25:75) were purchased from Daigang Bioengineering Co., Ltd. (Jinan, China). Anhydrous ethanol (AE), tetrahydrofuran (THF), and 3-aminopropyl triethoxysilane (APTES) were purchased from McLean Biochemical Technology Co., Ltd. (Shanghai, China). SBF (pH 7.4) was freshly prepared prior to use [50].

2.2. Preparation of the MgF_2-PA-PLGA composite coating

The preparation procedure of the "build-up" composite film is shown in Fig. 1A. Firstly, the ZM21 stents or sheets were immersed in 40% HF solution under shaking (300 r/min) at 25 °C for 8 h. Then, the samples were ultrasonically cleaned with AE for 5 min and desiccated using a vacuum oven. Subsequently, the PTMC and APTES solutions were co-sprayed onto the MgF_2 surface to obtain PTMC/APTES composite coatings. Briefly, PTMC (1 mg/mL in THF) and APTES (1% in AE) solutions were filtered using a 0.45 μm filter. Then, the two solutions were filled into two individual syringes and placed on micro syringe pumps. The feeding speeds of PTMC and APTES solutions were 0.05 and 0.01 mL/min, respectively, and 20 spraying cycles were processed. After spraying, the samples were dried in a vacuum oven at 100 °C for 1 h. The PTMC/APTES composite coating-covered samples were named MgF_2-PA. Finally, the PLGA coating was deposited on MgF_2-PA. Briefly, PLGA was dissolved in THF (2 mg/mL) and filtered using a 0.45 μm filter. Then, the solution was sprayed onto MgF_2-PA with a feeding speed of 0.035 mL/min for 20 cycles. Afterwards, the samples were dried in a vacuum for 1 h at 37 °C and stored for future use. The obtained PLGA covered MgF_2-PA and was named MgF_2-PA-PLGA. Simply put, the "build-up" composite film consists of a bottom MgF_2 conversion coating, a PA intermediate layer, and a PLGA top layer. PLGA was prepared by spraying PLGA on the surface of bare stents, and PTMC, APTES, and PLGA were sprayed on the surface of MgF_2 to prepare MgF_2-PTMC, MgF_2-APTES, and MgF_2-PLGA as control samples.

2.3. Material characterizations

The chemical characterization of the stents was performed by energy dispersive spectroscopy (EDS) in area scan mode with an acceleration voltage of 10 kV. EDS analysis was carried out in two locations: the first was scanned at low magnification to determine element distribution, and the second was scanned at high magnification to evaluate element content. The molecular structures of MgF_2, MgF_2-PTMC, MgF_2-APTES, MgF_2-PLGA, MgF_2-PA, and MgF_2-PA-PLGA composite coatings were measured by a Fourier transform infrared spectrometer (Nicolet 5700, Nicolet Inc., USA). High-resolution scanning electron microscopy (SEM) images of the PA coating were obtained using a JSM-7800F Prime instrument (JEOL Ltd., Japan). SEM and a stereo microscope (NSZ-608T, Nanjing Jiangnan Novel Optics Co., Ltd., China) were used to observe the microscopic morphology of the coating after the stent was crimped and expanded to a diameter of 2.75 mm. To measure the coating thickness, the stents were first cut out using microscissors, then the cross-sections were exposed by mounting the samples vertically to the

Table 1
Chemical composition of the ZM21 Mg alloy.

Elements	Zn	Mn	Mg
wt.%	1.7607	0.4519	Bal.

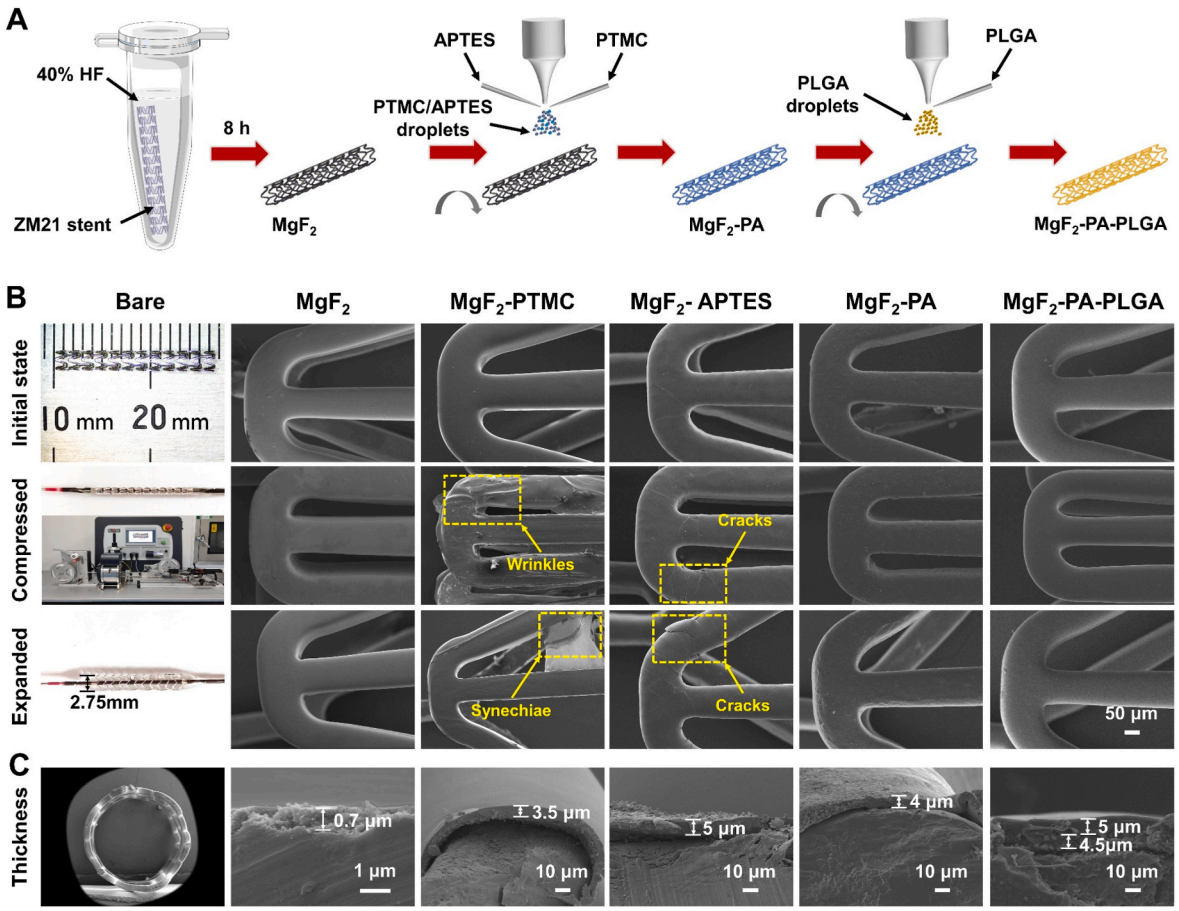

Fig. 1. (A) Schematic diagram for preparing MgF_2-PA-PLGA composite coating on ZM21 stents. (B) The surface morphology of the coatings after compression and expansion. (C) SEM images of strut cross-sections.

stage. All samples were sputtered gold with a 15 nm thickness before SEM evaluation. The process of compressing and expanding the stent is displayed in Fig. 1B. The stent was first compressed with a radial pressure of 90 N using a stent compression station (Model CX with Autosheath and Alpha-Crimp™, BlockWise, USA), and then expanded with a balloon pressure pump (JYLB-01, Shenzhen Jinchengrui Medical Technology Co., Ltd., Chain) under 12 atm water pressure. The radial support force of the ZM21 stents was tested with an electronic universal testing machine (AGS-X 2 kN, Shimadzu, Japan) at a loading rate of 1 mm/min.

2.4. In vitro degradation test

Mg corrodes in aqueous solution generally according to the following reaction formula:

$$Mg + 2H_2O \rightarrow Mg(OH)_2 + H_2 \quad (1)$$

Consequently, the release of hydrogen can be used to calculate the corrosion rate of Mg alloys. Static hydrogen collecting devices were used to assess the stents' hydrogen evolution rate [9] with a 0.05 ml resolution for the detection of gas generation at very low levels. A Tris/HCl buffered SBF solution was chosen as the corrosion medium to evaluate the *in vitro* degradation behavior of stents to simulate the blood vessel environment [50]. Before the test, all the stents were crimped with 90 N radial pressure on a balloon delivery system (2.75 × 18 mm), followed by full dilatation with 12 atm pressure. Unless otherwise mentioned, the same compression and expansion procedures were performed for all tests. As shown in Fig. 3A and Figs. S1–C, the expanded stents were fixed in the hydrogen evolution collection devices using fishing lines and immersed in 250 mL of SBF solution for 1, 2, 4, 7, 14, and 21 days at 37 °C. The relative mass loss of the stent is calculated according to the following formula [47,51]:

$$Mass\ loss = [(V / V_m) \times M] / M_0 \times 100\% \quad (2)$$

where V is hydrogen volume in L; V_m = 22.4 L/mol, representing the molar volume of gas at standard temperature and pressure conditions; M = 24.305 g/mol, which is the relative atomic mass of Mg; and M_0 is the initial mass of the stent in g.

The *in vitro* corrosion rate of the stent is calculated using the following equation [47,51]:

$$P_H = 2.279 \times V_H \quad (3)$$

where:

V_H = volume (ml)/surface area (cm^2)/days, the surface area of the stent is 1 cm^2, and.

P_H = mm/year.

The morphology and remaining radial support force of stents after immersion were determined by SEM, stereomicroscopy, and an electronic universal testing machine, respectively. On the 2nd, 4th, 6th, 8th, 10th, 14th, and 21st days of stent corrosion, 5 ml of stent corrosion solution was collected respectively, and the Mg^{2+} concentration was detected by atomic absorption spectrometry (TAS-990, Beijing Purkinje General Instrument Co., Ltd.).

2.5. Cytotoxicity and compatibility testing

The preparation of stent extracts was performed according to ISO 10993–5:2009 standards [52]. The prepared stents (30 each of PLGA,

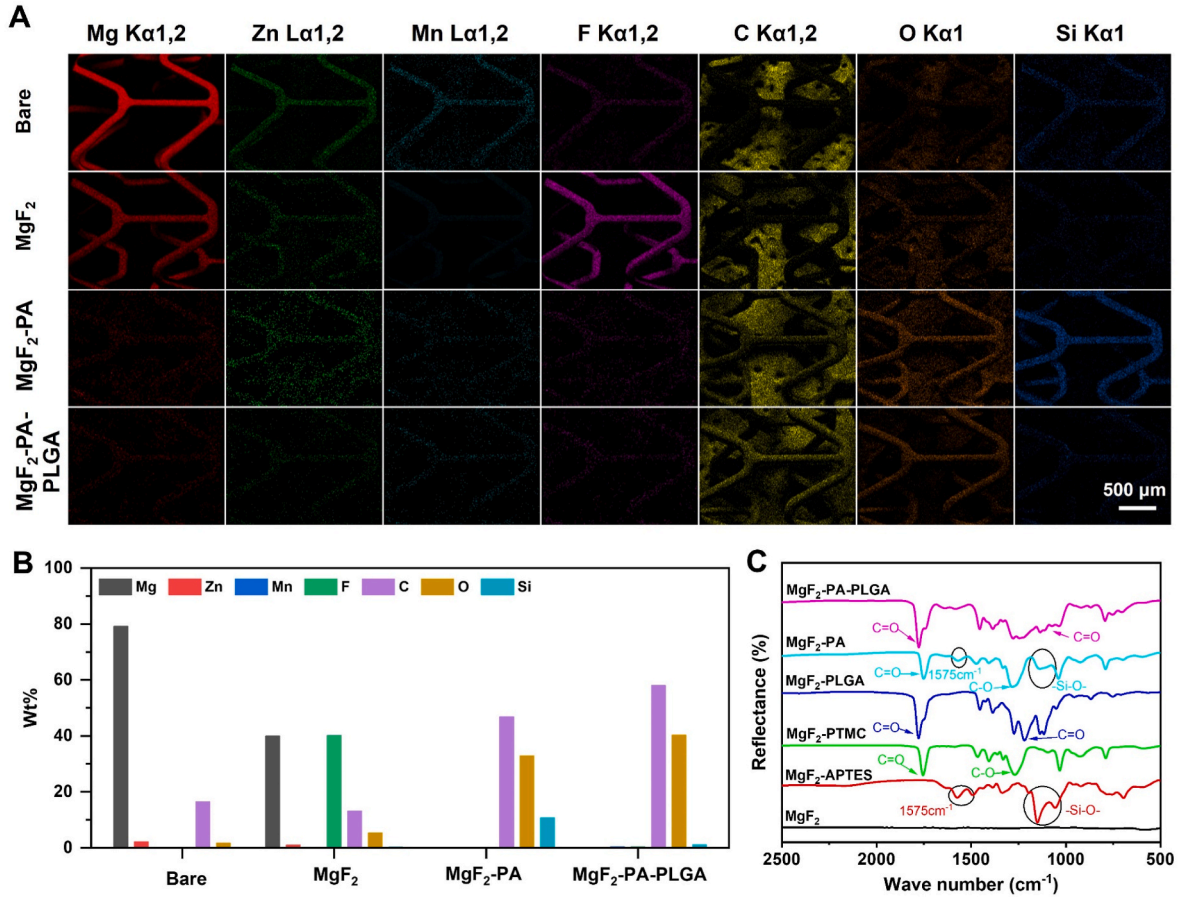

Fig. 2. The surface elemental map (A) and element mass ratio (B) of the bare ZM21, MgF_2, MgF_2-PA, and MgF_2-PA-PLGA stents obtained by EDS. (C) FT-IR diffuse reflection spectra of Mg samples coated with MgF_2, MgF_2-APTES, MgF_2-PTMC, MgF_2-PLGA, MgF_2-PA, and MgF_2-PA-PLGA.

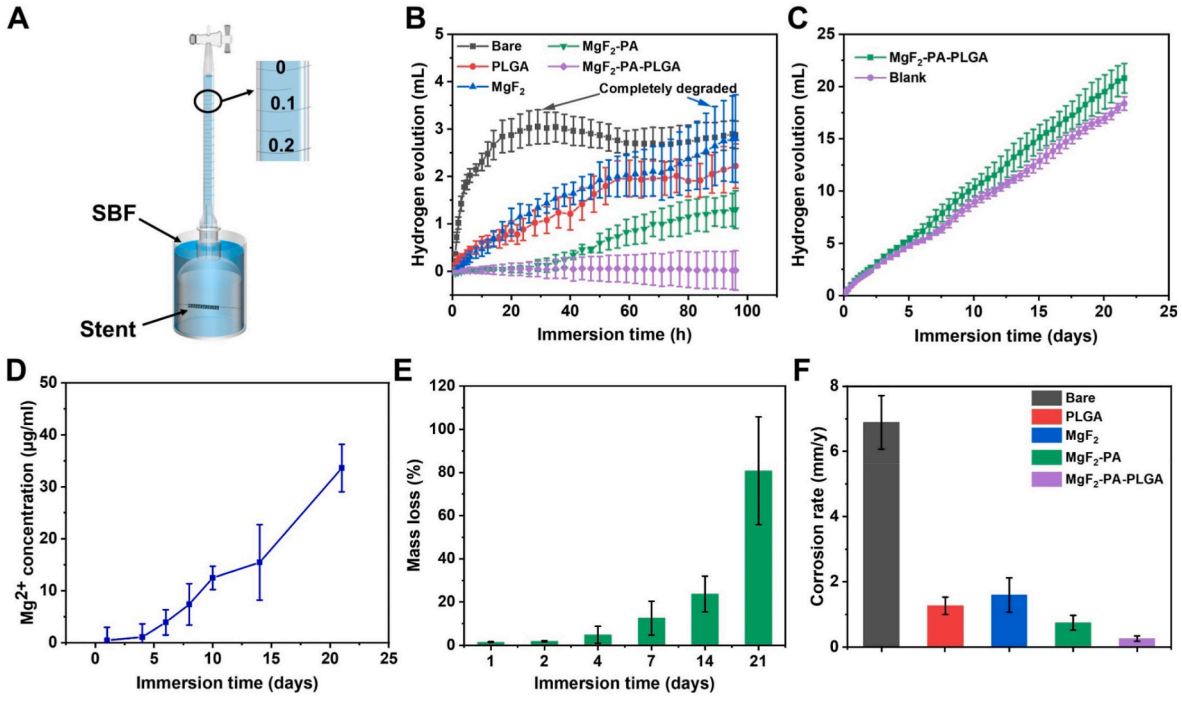

Fig. 3. *In vitro* corrosion evaluation of stents. (A) *In vitro* corrosion hydrogen collection device with ±0.05 ml resolution. (B) Hydrogen release curves after 96 h of immersion for Bare, PLGA, MgF_2, MgF_2-PA, and MgF_2-PA-PLGA. (C) Hydrogen release behavior of the blank group and MgF_2-PA-PLGA-coated stents immersed for 21 days. (D) Mg^{2+} concentration of MgF_2-PA-PLGA stents at different immersion time points. (E) Mass loss of stents with MgF_2-PA-PLGA coating that were immersed for 1, 2, 4, 7, 14, and 21 days. (F) Corrosion rates of Bare, PLGA, MgF_2, MgF_2-PA, and MgF_2-PA-PLGA *in vitro*.

MgF_2, MgF_2-PA, and MgF_2-PA-PLGA) were divided into two groups and put into four centrifuge tubes containing 30 ml of endothelial cell culture medium (ECM, ScienceCell, US) and smooth muscle cell culture medium (SMCM, ScienceCell, US) respectively, and the extracts were collected after 24 h of incubation at 37 °C.

In the cell culture experiment, human umbilical vein endothelial cells (HUVECs) and human umbilical artery smooth muscle cells (HUASMCs) purchased from Guangzhou Geneo Biotech were first subcultured and then seeded in 24-well plates at a density of 1.5×10^4 and 2×10^4 cells/ml, respectively. After incubation at 37 °C and 5% CO_2 for 1 day, the medium was removed, and 1 ml of extract was added to the corresponding wells according to the grouping. The cells cultured with ECM and SMCM medium without extract were used as the control group. The HUVECs and HUASMCs added with different extracts were incubated at 37 °C with 5% CO_2 for 1, 3, and 5 days, and the cells cultured for 3 and 5 days were replaced with new medium and extracts when they were cultured for 1 and 3 days, respectively. After incubation, the culture medium and extraction solution in the well plate were removed, rinsed with 0.9% saline three times, and 300 μL of fresh culture medium consisting of 90% complete medium and 10% CCK-8 reagent were added to each well. The cells were then incubated for 1 h. Subsequently, 200 μL of the supernatant were collected and transferred into a 96-well plate, and the absorbance value at 450 nm was detected with a microplate reader (Epoch 2, BioTek, VT, USA). The following is a detailed calculation of cell viability [53]:

$$Cell\ viability = [(As - Ab) / (Ac - Ab)] \times 100\% \quad (4)$$

where:

As = OD value of the experimental wells; Ab = OD value of blank wells; Ac = OD value of control wells.

The cells in the 24-well plate were fixed with 3% glutaraldehyde at room temperature for 2 h, stained with rhodamine 123, and photographed by fluorescence microscopy (Axio Observer Z1, Carl Zeiss, Germany).

2.6. Semi-in vivo and In vivo hemocompatibility

Semi-in vivo as well as short-term implantations of the stent were performed in order to further evaluate the hemocompatibility of the MgF_2-PA-PLGA stent. *Semi-in vivo* experiments were performed using an arteriovenous shunt model that had previously been reported [54]. Before the experiment, New Zealand white rabbits (3–3.5 kg) purchased from Chengdu Dashuo Laboratory Animal Technology Co. were anesthetized by intravenous injection of pentobarbital sodium (30 mg/kg). The extracorporeal circuit was established by connecting the left carotid artery and the right external jugular vein of New Zealand white rabbits, and the 316L stainless steel (SS) stent, PLGA, MgF_2, MgF_2-PA, and the MgF_2-PA-PLGA stent were compressed and implanted in the middle of the extracorporeal circuit (Fig. 8A). After 2 h of blood circulation, the experiment was terminated, the cross-section of the tube containing the stent was photographed, and the patency rate was calculated. After that, the stent-containing tubes were fixed overnight in a 2.5% glutaraldehyde solution and subjected to gradient dehydration and drying. The mass of the thrombus was calculated by extracting the stent from the tube and weighing it prior to analysis by SEM.

In order to further evaluate the hemocompatibility of the stent *in vivo*. 316L SS and MgF_2-PA-PLGA stents were respectively implanted in the iliac arteries of New Zealand white rabbits (Fig. 8F). Blood vessels containing stents were collected 2 h after implantation and fixed with 2.5% glutaraldehyde for 24 h, then dehydrated, dealcoholized, and critical point dried for SEM observation.

2.7. In vivo long-term implantation of stents

Twelve adult male New Zealand white rabbits (3–3.5 kg) were used for stent implantation. The rabbits were divided into three groups according to the time of implantation. Bare ZM21 stents and MgF_2-PA-PLGA stents were individually crimped onto 2.75 × 18 mm balloon delivery systems and sterilized by ethylene oxide. Before implantation, rabbits were anesthetized with an intravenous injection of sodium pentobarbital (30 mg/kg). Then, both bare ZM21 stents and MgF_2-PA-PLGA stents were delivered to the left and right iliac arteries by puncturing, respectively. During implantation, the balloon pressure was 12 atm for 40 s. The rabbits were euthanized after 1, 3, and 6 months of implantation, and the arteries containing stents were harvested for micro-CT, SEM, and histological analysis. All animal experimentation procedures complied with the Guide for the Care and Use of Laboratory Animals and the Regulations on the Administration of Laboratory Animals of Southwest Jiaotong University.

2.8. Histological analysis

Harvested arteries containing bare ZM21 and MgF_2-PA-PLGA stents were randomly selected for morphological and histological evaluation. The stented arteries were cut into two equal sections along the transverse direction. One section was further longitudinally halved and fixed in 2.5% glutaraldehyde for 24 h, then dehydrated, dealcoholized, and critical point dried for SEM observation. The other half was fixed in 4% paraformaldehyde solution for 4 h at room temperature, then dipped in 0.5% Triton X-100 solution in PBS for 30 min, then blocked with 1.5% BSA in PBS at 4 °C for 12 h. After incubating in mouse anti-rabbit CD31/PECAM-1 antibody solution (Novus Biologicals, 1:200 dilution with 1.5% BSA) and goat anti-mouse IgG-Alexa Fluor® 488 secondary antibody solution (BIOSS, 1:200 dilution with 1.5% BSA) for 12 h at 4 °C, the stented artery was stained with phalloidin-TRITC (1:40 dilution with 1.5% BSA) and 4',6-diamidino-2-phenylindole (DAPI, dilute to 1 μg/mL with 1% BSA) for 24 h and 10 min, respectively, then observed using a Laser Scanning Confocal Microscope (A1 Plus, Nikon, Japan) and analyzed with NIS-Elements Viewer Software (NIS-E 4.5, Nikon, Japan). The other transversely halved section was fixed for 24 h in 4% paraformaldehyde and then embedded in paraffin. The embedded artery was sliced at 5 μm intervals and cut into five slices. Subsequently, the samples were stained with hematoxylin-eosin (H&E), photographed, and analyzed using a light microscope (CKX41, OLYMPUS, Japan).

2.9. Micro-CT analysis

The MgF_2-PA-PLGA stents at different time points (1, 3, and 6 months) were scanned using a μCT 100 (SCANCO Medical micro-CT systems, Switzerland) with a scanning resolution of 6.6 μm (70 kV, 114 μA, 230 ms). Mimics Research 21.0 software was used to reconstruct three-dimensional images and calculate the volume of stents and corrosion products.

2.10. Statistics and data analysis

All experimental results are expressed as mean ± standard deviation (SD). More than three independent samples were used for each test. Statistical analysis was performed using SPSS 18.0 software (SPSS Inc., Chicago, USA) by one-way ANOVA of variance. *$p < 0.05$ was considered a significant difference between groups.

3. Results

3.1. Characterization of the coatings

3.1.1. Microstructure and mechanical properties of the coatings

The degradation rate of a Mg alloy BRS is determined by the coating's performance [55]. To comprehensively evaluate the mechanical properties of several coatings, SEM was used to characterize the thickness and surface morphology of the coatings after compression and

expansion (Fig. 1B and C). The results showed no obvious deformation or detachment of the MgF_2 coating during compression and expansion, implying good mechanical properties of the MgF_2 coating. While wrinkles and synechiae appeared after compression and expansion of the PTMC coating. This was mainly caused by the poor stiffness and viscosity of PTMC. By contrast, the APTES coating maintained a continuous and smooth surface morphology after compression with only a few small-sized ruptures. Nevertheless, the number of these cracks increased significantly, and part of the coating detached from the substrate after expansion. These results indicated that pure APTES and PTMC coatings both have poor mechanical properties, leading to severe defects during stent deformation. Defects in the coating could weaken its protective effect and induce localized corrosion [56]. Noticeably, the MgF_2-PA coating combined the stiffness and stickiness of PTMC and APTES, retaining its shape without cracking throughout the compression and expansion processes. This shows the synergistic function between PTMC and APTES. In comparison to the MgF_2-PA coating, the surface morphology of the "built-up" composite film was smoother and also had excellent compression and expansion properties.

The cross-sectional images showed a dense MgF_2 conversion layer with a thickness of 0.75 μm formed on the stent surface. In MgF_2-PTMC, MgF_2-APTES, MgF_2-PA, and MgF_2-PA-PLGA, the coating thicknesses of PTMC, APTES, PA, and PA-PLGA were 3.5 μm, 5 μm, 4 μm, and 9.5 μm, respectively. The MgF_2 coating was not visible in other coatings due to its low thickness [57]. Even though the sample preparation process left a tiny gap between the coating and the substrate, the evaluation of the compression and expansion characteristics of the "built-up" composite film shows the coating's excellent adherence to the substrate.

3.1.2. Chemical characterization of the coating

Fig. 2A shows the surface elemental maps of ZM21, MgF_2, MgF_2-PA, and MgF_2-PA-PLGA stents, and the corresponding atomic mass ratios are shown in Fig. 2B. Mg, Zn, Mn, C, and O are clearly visible on the surface of ZM21. C and O may be caused by surface oxidation or alcohol residues left during stent polishing. The homogeneous distribution of F elements on the MgF_2 stent surface implies that the MgF_2 film was successfully prepared. The Si in APTES emerged on the surface of the MgF_2-PA stent, whereas the F element was very faint, implying that the MgF_2 had been covered by the PA coating. Furthermore, a trace quantity of Si was detected on the surface of the MgF_2-PA-PLGA stent, illustrating that the PLGA entirely encapsulated the MgF_2-PA.

The FT-IR spectra of each material utilized to prepare the composite coating are displayed in Fig. 2C. No characteristic peak was observed on MgF_2 substrates. The MgF_2-APTES sample clearly showed a peak around 1045 cm^{-1}, corresponding to Si–O asymmetric stretching in -*Si*-O-Si- [58,59]. The peak at 1590 cm^{-1} was mainly caused by the protonated amino groups from APTES's successful bonding. In addition, APTES forms covalent connections with MgF_2 substrates due to hydroxyl groups [36,48]. The peaks of MgF_2-PTMC coating at 1750 cm^{-1} and 1270 cm^{-1} correspond to the C═O and C–O stretching vibration characteristic peaks of PTMC, respectively [39]. The presence of the PLGA layer is confirmed by the C═O stretching at 1775 cm^{-1} and the C–O stretching at 1215 cm^{-1} in the MgF_2-PLGA coating [1,60,61]. In the MgF_2-PA coating, the characteristic peaks of PTMC and APTES are seen, but not in the MgF_2-PA-PLGA coating. However, the C═O stretching at 1775 cm^{-1} and the C–O stretching characteristic peak at 1215 cm^{-1} for PLGA were seen in the MgF_2-PA-PLGA coating. Furthermore, this solid polysiloxane network with exposed amine functional groups not only promotes adhesion to substrates but also enhances bond strength by forming hydrogen bonds with PTMC and PLGA [39,60]. In order to study the mixed structure of the PA coating further, 1 mg/ml PTMC, 1% APTES, AE, and THF were mixed two by two. As shown in Figs. S1–A, precipitation formed after the addition of APTES solution or AE to the PTMC solution. Nevertheless, no precipitation occurred after adding THF to the APTES solution. This reveals that PTMC is AE-insoluble. As shown in Figs. S1–B, the PA coating has a microphase separation structure. The EDS results show that the continuous phase has a higher silicon content, indicating that the continuous phase is APTES. Additionally, when PTMC and APTES were co-sprayed on the surface of the stent, THF evaporated quicker than AE, causing PTMC to precipitate in AE and form a microphase-separated structure. The above results revealed that the "built-up" composite film was successfully prepared on the material's surface.

3.2. In vitro corrosion behavior

3.2.1. Hydrogen release rate

The *in vitro* degradation rates of bare ZM21 and modified stents were evaluated by a hydrogen release detection device. The upgraded hydrogen evolution device is an inverted cylindrical funnel that can contain more electrolytes and increase the ion exchange of the solution around the bracket. Moreover, the gas volume resolution of 0.05 mL allows for the detection of tiny gas changes (Figs. S2–D). In the corrosion assessment, a blank group was included to eliminate the impact of the solution itself on the hydrogen release rate. The hydrogen release curves of the PLGA-coated stents are shown in Figs. S2–A. The protective effects of three molecular weight PLGAs on bare stents did not vary significantly. As shown in Figs. S2–B, bare ZM21 stents had the highest hydrogen release rate, whereas stents coated with MgF_2, PLGA, MgF_2-PA, and MgF_2-PA-PLGA had gradually decreased release rates. The gas release curves of the MgF_2-PA-PLGA stent and the blank group were almost identical, revealing that the "built-up" composite film stents basically did not corrode during four days of immersion.

Fig. 3B displays the hydrogen release curves of the stents in each group after blank-correction. It is obvious that the MgF_2-PA-PLGA-coated stents did not release substantial hydrogen after immersion for 4 days. The curve reached a plateau after 24 h of immersion, suggesting that the bare ZM21 stents had degraded entirely. MgF_2 stents and PLGA stents prolonged the period of degradation to 4 days in comparison to bare stents, whereas MgF_2-PA stents dissolved around 50% after 4 days of immersion. Fig. 3C shows that the MgF_2-PA-PLGA stents had almost no hydrogen release during the first seven days of immersion, but that the quantity of hydrogen release steadily increased over the seventh through twenty-first days of immersion. This indicates that the MgF_2-PA-PLGA stents degrade as immersion time increases. Fig. 3D shows the Mg^{2+} release rate of the MgF_2-PA-PLGA stents at various time periods during immersion. The amount of Mg^{2+} released in the solution steadily increases as the immersion period increases. At the same time, the mass loss data in Fig. 3E revealed that the stent's mass loss was maintained at a low level throughout the early stage of immersion and increased significantly from 14 to 21 days. In addition, Fig. 3F depicts that the MgF_2-PA-PLGA stent has the lowest corrosion rate of 0.26 ± 0.08 mm/y, whereas the bare stent, PLGA, MgF_2, MgF_2-PA, and MgF_2-PA-PLGA have corrosion rates of 6.89 ± 0.82, 0.74 ± 0.23, 1.26 ± 0.27, and 1.60 ± 0.52 mm/y, respectively. The above results indicate that the "built-up" composite layer has an excellent corrosion control function on the bare stent.

3.2.2. Corrosion morphology

The corrosion morphologies of bare ZM21 stents and modified stents after immersion in SBF for 4 h, 1 day, 2 days, 4 days, 14 days, and 21 days are shown in Fig. 4. The macro-corrosion morphology is shown in Fig. 4A. After immersion for 4 h, the bare stents were severely corroded, and the majority of the stent struts were broken. The corrosion resistance of the modified stent was significantly improved compared to the bare stent. The MgF2 stent retained its physical structure during the first two days of immersion, but it was completely dissolved by the fourth day. The MgF_2-PA stent still had a relatively complete structure after 4 days, but some areas were seriously corroded. However, when the MgF2-PA-PLGA stent was immersed on the 14th day, it still retained the complete structure, indicating that the MgF2-PA-PLGA coating had excellent corrosion protection on the ZM21 stents. The MgF2-PA-PLGA

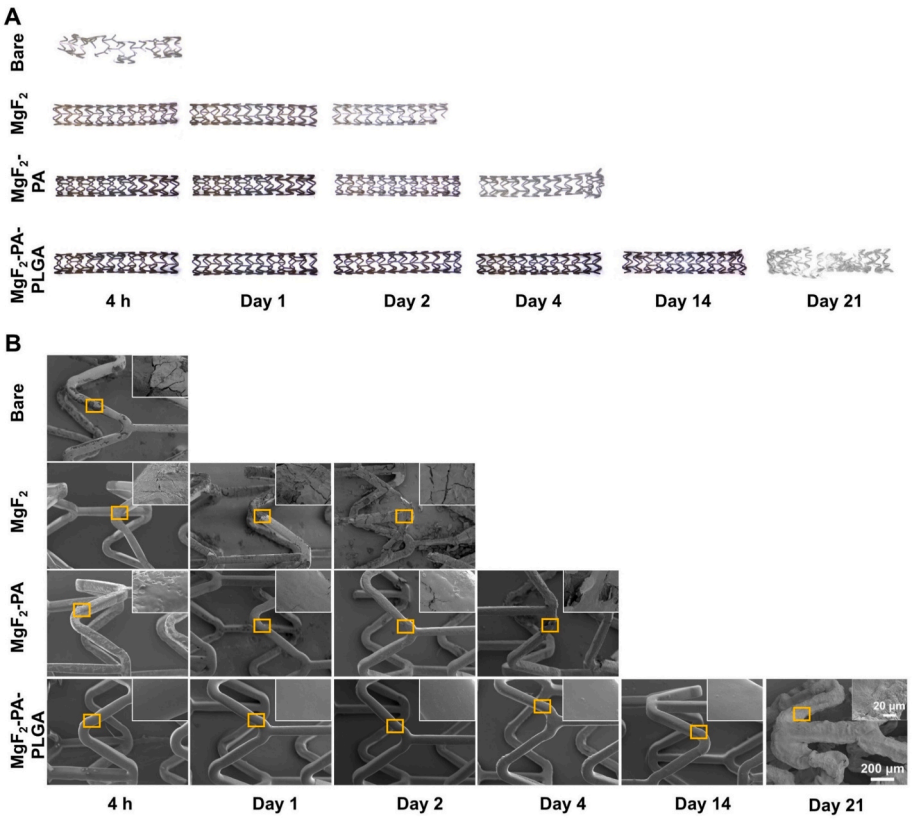

Fig. 4. Corrosion morphologies of stents *in vitro*. (A) Macro morphology of stent after immersion at different time points. (b) SEM images of stents immersion at different time points. Insets are magnified images of the yellow rectangular area. (The empty area indicates that the stent has completely degraded.)

stent, however, was severely corroded after 21 days of immersion, indicating that the stent exhibited accelerated corrosion from the 14th to the 21st day of immersion.

The microscopic corrosion morphology is shown in Fig. 4B, which is consistent with the results of the macroscopic morphology. Many cracks appeared on the surface of the bare ZM21 stent after immersion for 4 h, which indicated that the stent had undergone severe crevice corrosion. The same phenomenon also occurs after immersion of the MgF2 stent for 1 day. It is clearly seen that the most serious corrosion is in the bending part of the stents. On the contrary, the coating on MgF2-PA-PLGA stents did not have obvious cracking phenomena even after immersion until the 14th day. However, severe corrosion occurred on the surface of the MgF2-PA-PLGA stent after 21 days of immersion, and the stent struts were distorted. This clearly displays the "built-up" composite film's excellent corrosion control effects, as well as the synergistic functions of the MgF2, PA, and PLGA coatings.

The cross-sections of the stents immersed at different times were evaluated by SEM in order to reflect the overall corrosion morphology more accurately. Furthermore, the stress concentration area is enlarged and analyzed (Fig. 5A). The results demonstrate that all of the stents exhibit a more severe tendency to corrosion in the stress concentration area than in other regions [62,63]. After 14 days of immersion, the MgF_2-PA-PLGA stents still had their full physical structure, but the protective coating at the stress concentration location had decreased, which is also shown in Fig. 5B. However, after 21 days of immersion, the stent structure was distorted, and more severe corrosion occurred in the stress concentration region. This indicates that during long-term immersion of a stent, the preferential corrosion sites seem to be the bending sections, or stress concentration sites. *In situ* corrosion of expanded and unexpanded MgF_2-PA-PLGA stents confirmed this hypothesis (Fig. 5B). During a 21-day immersion, the unexpanded stents exhibited no corrosive signs. Nevertheless, the number of corrosion sites on the MgF_2-PA-PLGA stent increased on the 14th day of immersion, and the corrosion area expanded further after 21 days of immersion. This phenomenon clearly illustrates that the stent's compression and expansion significantly influence the coating, particularly at the locations of stress concentration. Furthermore, despite the fact that corrosion sites were observed in the MgF2-PA-PLGA stents after 14 days of immersion due to stress concentration, compared to bare ZM21 stents, the corrosion resistance of MgF2-PA-PLGA stents *in vitro* was substantially superior. This is sufficient evidence that the "built-up" composite film stent has outstanding corrosion control effects *in vitro*.

3.2.3. *Radial strength*

The surface morphology of the stent after corrosion can only reflect the stent's local corrosion degree and hardly reveal changes in the stent's mechanical characteristics. As a result, it is necessary to evaluate the radial support force of the stents after corrosion. Fig. 6 depicts the variations in radial support force of the stents after different immersion times. It can be seen that the bare stent completely lost its supporting force after immersion for one day, while the supporting force of the MgF2 stent and the MgF2-PA stent dropped sharply after two days of immersion. On the fourth day, the supporting force of the MgF2-PA stent was less than 40% of the initial supporting force (Fig. 6C). The predominant cause of the decrease in supporting force of MgF_2-PA coated stents after 4 days of immersion was the rapid breakdown of the coating and the occurrence of localized corrosion spots (Fig. 5A). Fig. S2-C reveals that the supporting force of the MgF2-PA-PLGA stent decreases in a linear way, and even after 21 days of immersion, 16% of the supporting force persists, demonstrating once again the MgF2-PA-PLGA coating's exceptional corrosion control effects.

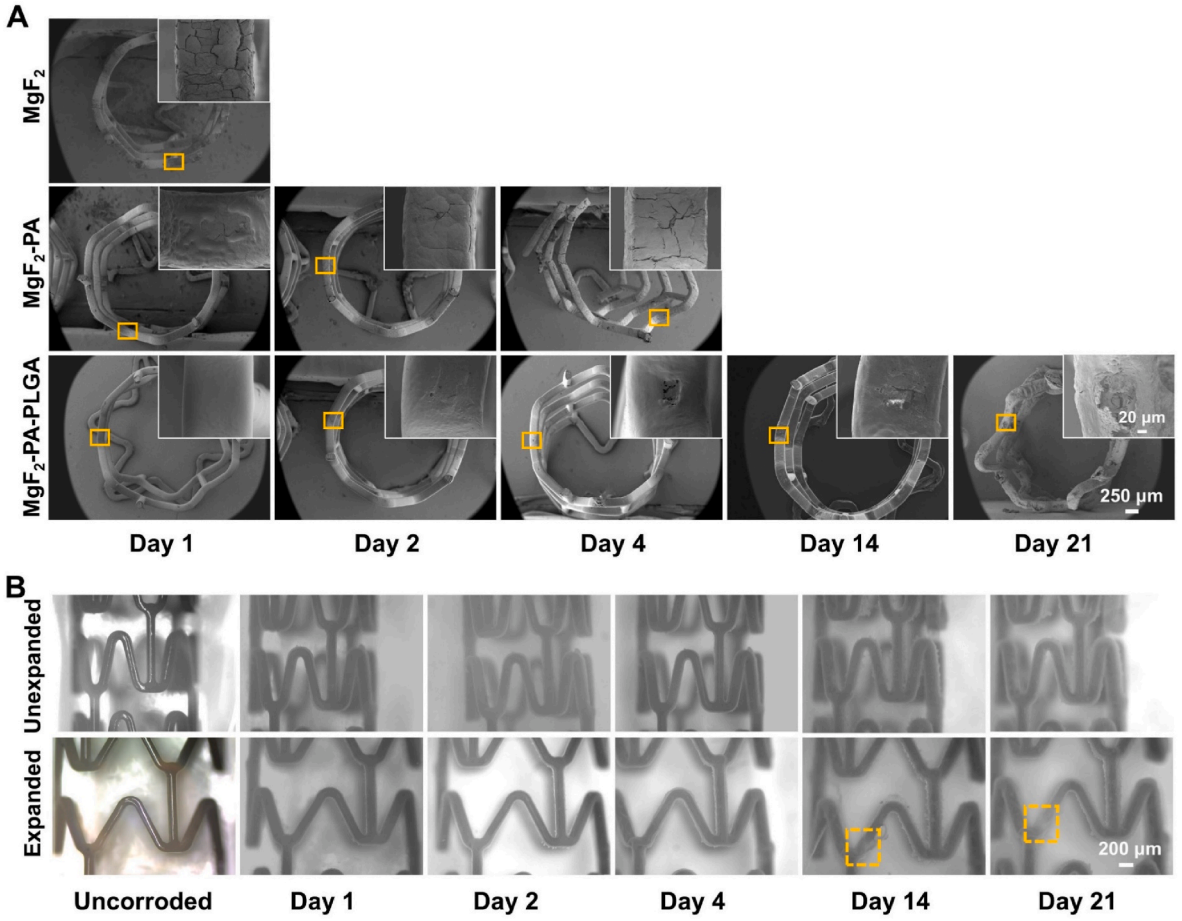

Fig. 5. The cross-sectional photographs (A) and *in situ* corrosion morphologies (B) of stents after immersion at different times. (A) The cross-sectional SEM images of stent immersion for 1, 2, 4, 14, and 21 days. Insets are magnified images of the yellow rectangular area. (B) *In situ* corrosion morphologies of stents prior to corrosion, immersion for 1, 2, 4, 14, and 21 days. The area in the yellow dashed box indicates the occurrence of localized corrosion. (The empty area indicates that the stent has completely degraded.)

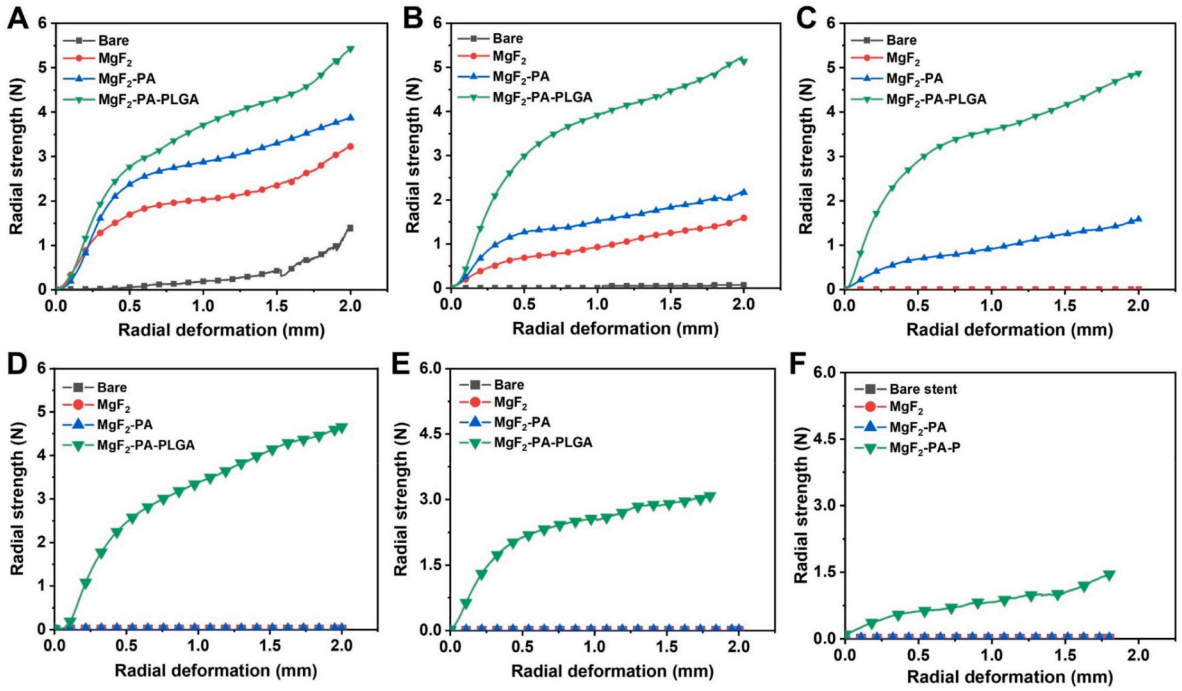

Fig. 6. Radial support force of stents after immersion at different time points. (A) 1 day. (B) 2 days. (C) 4 days. (D) 7 days. (E) 14 days. (F) 21 days.

3.3. Cytocompatibility and hemocompatibility

3.3.1. In vitro cytocompatibility

Excellent biocompatibility is considered a prerequisite for the clinical application of implanted devices. As a result, we performed biological experiments *in vitro* on PLGA, MgF_2, MgF_2-PA, and MgF_2-PA-PLGA. As shown in Fig. 7A, there were no significant differences in the morphology of HUVECs cultured in the control group, PLGA, MgF_2, MgF_2-PA, and MgF_2-PA-PLGA extracts after 1, 3, and 5 days of incubation. The cell viability data (Fig. 7B) similarly revealed that there was no significant difference in the cell vitality of HUVECs in various groups after 1 day of culture. Although there was a significant difference in cell viability between the PLGA group and the control and MgF_2-PA-PLGA groups after 3 and 5 days of incubation, cell viability remained over 85%, indicating that PLGA, MgF_2, MgF_2-PA, and MgF_2-PA-PLGA extracts had no cytotoxicity to HUVECs. Fig. 7C shows the morphology, and cell viability data of HUASMCs cultured with PLGA, MgF_2, MgF_2-PA, and MgF_2-PA-PLGA extracts for 1, 3, and 5 days. Compared to the control group, MgF_2, MgF_2-PA, and MgF_2-PA-PLGA exhibited no discernible cytotoxicity.

3.3.2. Semi-in vivo and In vivo hemocompatibility

The morphology and cross-sectional images of the tube in Fig. 8 B revealed no severe thrombus formation or occlusion after 2 h of blood flow, but there was still a minor quantity of thrombus consisting of blood cells and reticular fibrin structures in local areas (Fig. S3). In addition, Fig. 8D shows that the clogging rate of PLGA, MgF_2, MgF_2-PA, MgF_2-PA-PLGA, and 316L SS after 2 h of blood circulation is less than 10%. The SEM images in Fig. 8E revealed that there were just a few round platelets on the surface of most sections of all stents.

Fig. 8G displays thrombus formation on the stent surface 2 h after the MgF_2-PA-PLGA and 316L SS stents were implanted in the iliac artery. There is no significant thrombus generation in the blood vessels implanted with MgF_2-PA-PLGA and 316L SS stents. However, a typical fibrous network structure emerged on the side of the stent's bending section, followed by local red blood cell accumulations. The turbulent flow at the bending location of the stent slows the blood flow at this site, which should be the primary cause of thrombus development [64]. The above results indicate that there are no significant differences in the hemocompatibility of PLGA, MgF2, MgF2-PA, MgF2-PA-PLGA, and 316L SS stents.

3.4. In vivo degradation behavior and biocompatibility

3.4.1. Micro-CT analysis

To evaluate the degradation behavior of the stents *in vivo*, bare stents and MgF_2-PA-PLGA stents were implanted into New Zealand white rabbit arteries. Three-dimensional images of MgF_2-PA-PLGA stents implanted at 1, 3, and 6 months were reconstructed by high-resolution micro-CT technology. Fig. 9 shows micro-CT images and the volume of Mg stents and corrosion products implanted at different time points. The MgF_2-PA-PLGA stent retained physical integrity during one month of implantation *in vivo* (Fig. 9A–i and A-ii), only a few points of the stent were corroded, and the corrosion locations were the bends of the stent structure (inset in Fig. 9A–i). This is consistent with the results of the *in vitro* corrosion. At three months, the MgF_2-PA-PLGA stent exhibited severe corrosion, especially at the stress concentration sites (Fig. 9A–iii), but the geometry of the stent was still recognizable. Moreover, the stent retracted significantly in the absence of blood pressure due to the lack of support force. At six months, the outline of the stent was no longer observable, except for some scattered corrosion particles and debris (Fig. 9A–v and 8A-vi).

Fig. 9B depicts the cross-sectional slices of the stented vessels. Homogeneous vessel walls and intact cross-sectional pictures of stent struts were found at 1 month. Three months after the MgF_2-PA-PLGA stents were implanted, the lumen was obviously lost, and the intima thickness

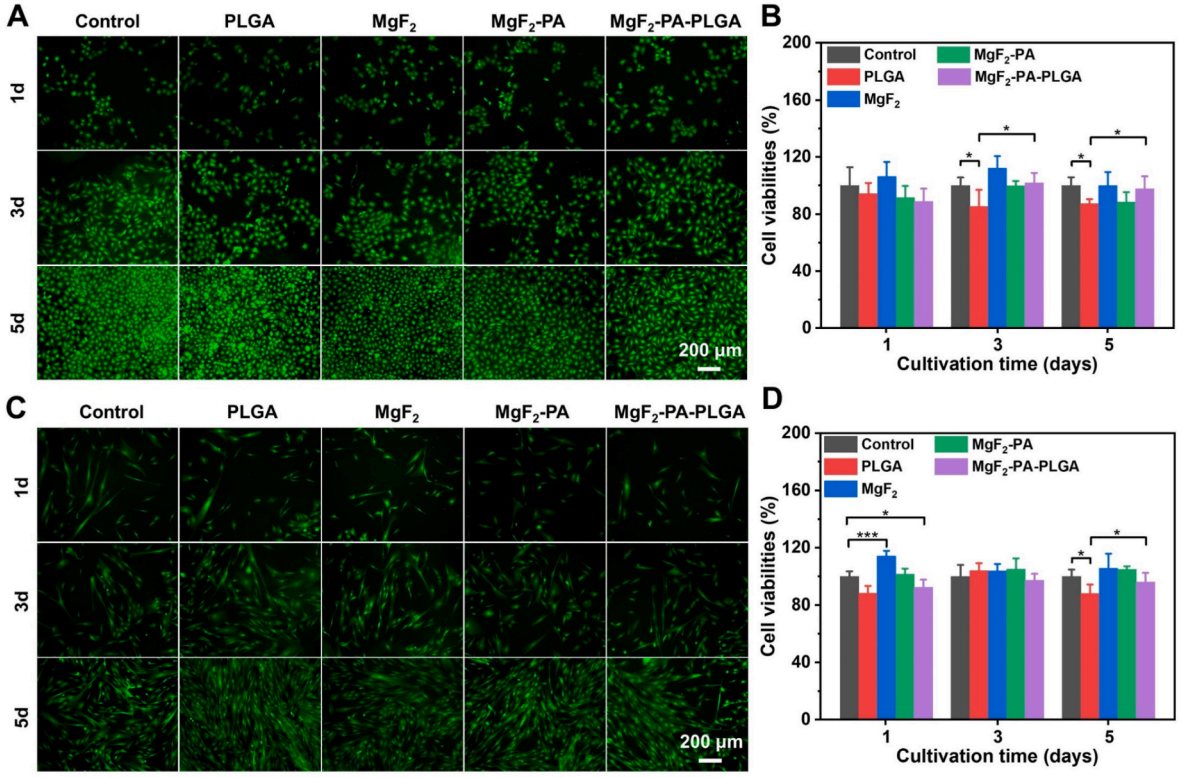

Fig. 7. (A) Fluorescent staining of HUVECs cultured for 1 day, 3 days, and 5 days. (B) HUVECs' viability after 1 day, 3 days, and 5 days of incubation is calculated from CCK-8 tests. (C) Fluorescent staining of HUASMCs cultured for 1 day, 3 days, and 5 days. (D) HUASMCs' viability after 1 day, 3 days, and 5 days of incubation is calculated from CCK-8 tests. Data are presented as mean ± SD (n = 4), *p < 0.05, **p < 0.01, ***p < 0.001, ****p < 0.0001.

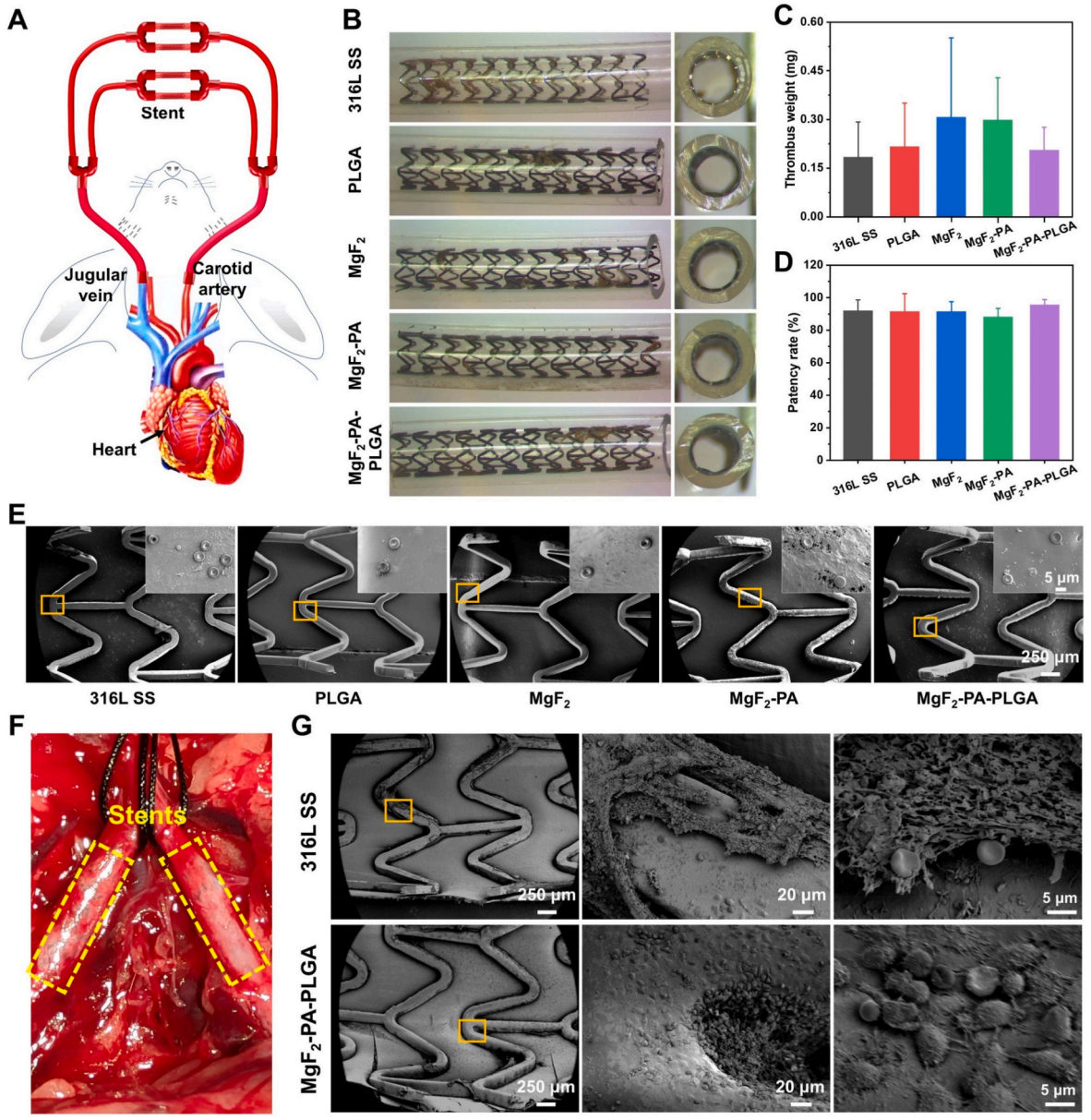

Fig. 8. *Semi-in vivo* and *in vivo* hemocompatibility of stents. (A) A schematic diagram of *semi-in vivo* animal experiments. (B) Cross-section and appearance morphology after 2 h of blood circulation without additional heparin. (C) Thrombus mass after 2 h of blood circulation. (D) Tube patency rate after 2 h of blood circulation. (E) SEM images of the stent after blood circulation for 2 h. Insets are magnified images of the yellow rectangular area. (F) Image exhibiting the implantation of stents in the left and right iliac arteries. (G) SEM images of MgF_2-PA-PLGA and 316L SS stents 2 h after *in vivo* implantation. Data are presented as mean ± SD (n = 4), *p < 0.05, **p < 0.01, ***p < 0.001, ****p < 0.0001.

increased, which may be related to the rapid degradation of the stents [65]. At six months, a few stent struts were seen. Volume changes of stents and corrosion products at different time points were calculated by grayscale adjustment in Mimics Research 21.0 software and are shown in Fig. 9C. At 1 and 3 months after stent implantation, the volume of corrosion products remained between 20% and 25%, implying that the degradation products were continuously absorbed [66]. The volumes of MgF_2-PA-PLGA stents were 82.6 ± 3.4%, 49.5 ± 10.6%, and 3.1 ± 0.2% after 1, 3, and 6 months after implantation, respectively.

Image J was used to determine the vessel wall thickness and lumen area from the CT scans. Consistent with the findings in Fig. 9B, the lumen was drastically reduced three months after implantation, decreasing from 4.3 ± 0.3 mm^2 at 1 month to 1.0 ± 0.1 mm^2 at 3 months, and the vessel wall thickness fell from 206.9 ± 43.9 μm to 391.7 ± 58.6 μm. At six months, the tendency was the opposite; the vessel wall thickness gradually decreased and the lumen area increased.

3.4.2. *Endothelialization analysis*

The surfaces of the MgF_2-PA-PLGA and bare ZM21 stents were covered entirely by tissue one month after implantation into the iliac arteries (Fig. 10A) with the structure of the stents still visible. The stent with the MgF_2-PA-PLGA coating retained its mechanical integrity, but the bare ZM21 stent corroded severely at its corners and lost mechanical recoil. To further evaluate the degree of endothelialization, immunofluorescence staining was performed on vessels containing MgF_2-PA-PLGA coating and bare stents implanted for 1 month (Fig. 10B). The results showed that the bare stent had fewer nuclei than the MgF_2-PA-PLGA stent. Also, both MgF_2-PA-PLGA-coated stents and bare stents showed CD31 expression, but MgF_2-PA-PLGA-coated stents had a denser and more intact endothelial cell layer.

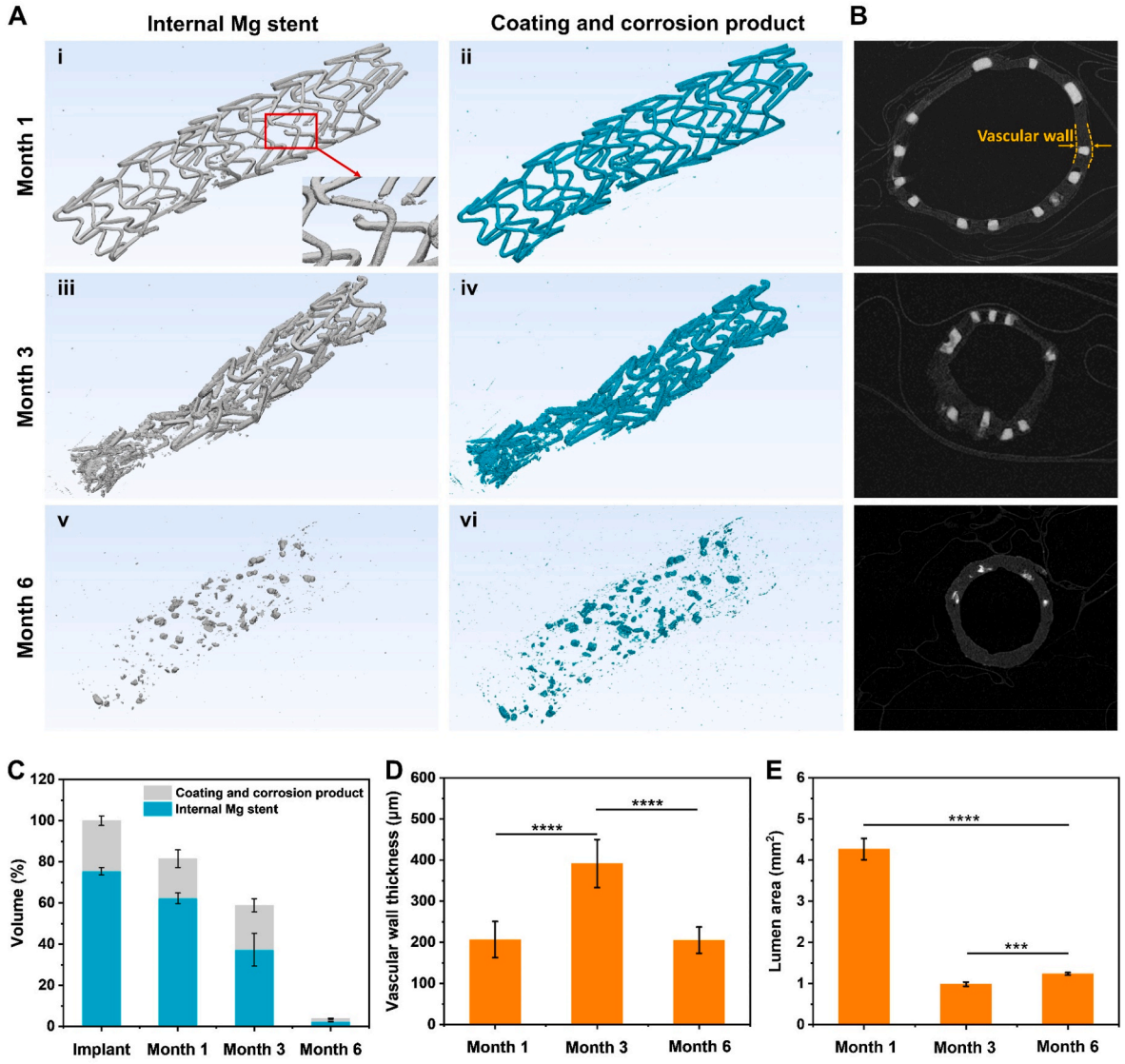

Fig. 9. Reconstructed 3D morphologies of MgF_2-PA-PLGA stents after implantation at 1, 3, and 6 months by high-resolution micro-CT. (A-i, A-ii) One month after implantation, degradation occurred in some sites. (A-iii, A-iv) Support was lost 3 months after implantation due to severe deterioration. (A-v, A-vi) Completely degraded 6 months after implantation. (C) The volume of MgF_2-PA-PLGA and corrosion products implanted at various times was calculated using Mimics Research 21.0 software. Changes of vascular wall thickness (D) and lumen area (E) at 1, 3, and 6 months of implantation. The data are presented as mean ± SD (n = 4), *p < 0.05, **p < 0.01, ***p < 0.001, ****p < 0.0001.

At 3 months, the MgF_2-PA-PLGA-coated stents were still visible, but the structure had deteriorated, whereas the bare stents were entirely invisible. The MgF_2-PA-PLGA-coated stent structures were not visible after 6 months, which is consistent with the micro-CT data stated above. Furthermore, the inner wall of the blood artery clearly showed oval endothelial cells growing in the direction of blood flow. This implies that the vascular tissue in the area where the stent was implanted has begun to remodel and that the stent did not have a negative effect on the blood vessel after complete degradation.

3.4.3. *Biocompatibility evaluation*

Histological techniques were used to evaluate the biocompatibility of MgF_2-PA-PLGA-coated stents and bare ZM21 stents (Fig. 11A). Some tissue was removed from its original place during tissue sectioning due to a mechanical mismatch between the stent struts and the paraffin-embedded tissue. At 1 month, the MgF_2-PA-PLGA-coated stents and bare ZM21 stents were wrapped in new tissue. Furthermore, the struts of the MgF_2-PA-PLGA stent were clearly visible, while some areas of the bare ZM21 stent had been corroded, and no obvious accumulation of corrosion products was found around the corroded struts.

At 3 months, the arteries implanted with bare ZM21 stents had more severe tissue hyperplasia than those implanted with MgF_2-PA-PLGA-coated stents. The bare stents dissolved completely 6 months after implantation, leaving no corrosion products. Similarly, only a few small particles of the MgF_2-PA-PLGA coated stents were discovered, and no corrosion products were detected in other regions. In-stent restenosis data (Fig. 11C) indicated that bare stents had a restenosis rate of 30 ± 7% at 1 month, compared to 9.2 ± 1.1% for MgF_2-PA-PLGA-coated stents. At three months after implantation, the restenosis rates for bare ZM21 and MgF_2-PA-PLGA-coated stents were 78.2 ± 4.1% and 59.1 ± 5.2%, respectively. At six months, the restenosis rates for both stents decreased to 70.8 ± 6.2% and 52.7 ± 6.9%, respectively. As shown in Fig. 11D, the lumen areas of the three-month stents were much smaller than those of the one-month stents, but they increased for the six-month stents. There were also significant differences in vessel wall thickness at different times after stent implantation. The vascular wall implanted with a bare stent and MgF_2-PA-PLGA stent was thinnest at 1 month, 401.8 ± 128 μm and 267.2 ± 78.7 μm, and thickest at 3 months, 668.8

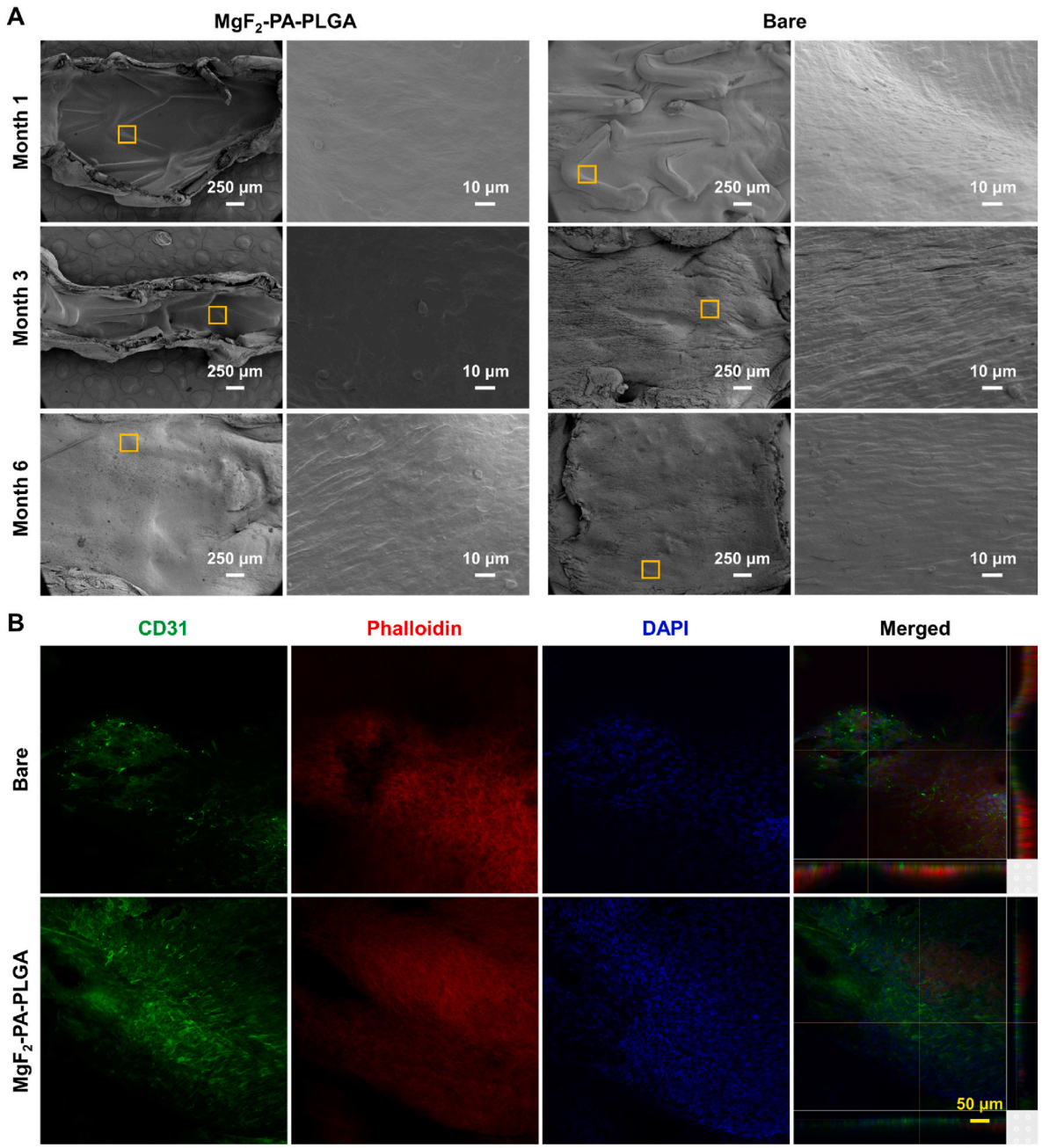

Fig. 10. (A) SEM images revealed the degree of endothelialization of MgF_2-PA-PLGA and bare ZM21 stents at 1 month, 3 months, and 6 months after implantation. (B) Confocal laser images to evaluate endothelialization 1 month after implantation of MgF_2-PA-PLGA and bare ZM21 stents.

$\pm$ 106.3 μm and 555.1 $\pm$ 111.3 μm, respectively (Fig. 11D). It decreased to 471.2 $\pm$ 68.2 μm and 474.3 $\pm$ 98.3 μm at 6 months, respectively. This indicates that the intimal proliferation has been alleviated with the degradation of the stents.

4. Discussion

Reasonable surface modification contributes to the improvement of the corrosion control effects and biocompatibility of the Mg alloy BRS. In this study, MgF_2-PA-PLGA "build-up" composite films were successfully prepared on the ZM21 BRS surface. The PA coatings formed by the co-spraying of PTMC and APTES exhibited excellent compression and expansion properties. The covalent bond between APTES and the substrate improves the adhesion of the PA coating with MgF_2 [36,48]. The PLGA on the top layer may also form hydrogen bonds with APTES to improve adherence to the PA coating [39,60].

The assessment of a biomedical implant must be performed under the most accurate service conditions. PTMC and APTES have shown superior corrosion resistance in prior studies [36,38]. However, different results were obtained when we sprayed individual PTMC and APTES onto the surface of ZM21 BRS. Despite the fact that the surface morphology was impeccable after spraying, the coating suffered substantial damage during compression and expansion (Fig. 1B). Flat samples were used in the majority of studies, resulting in the actual service environment of the stents being ignored. Compression and expansion are two essential steps of vascular stent implantation, which pose a high challenge to the coating's interfacial adhesion and mechanical characteristics. Excellent expanding properties have been

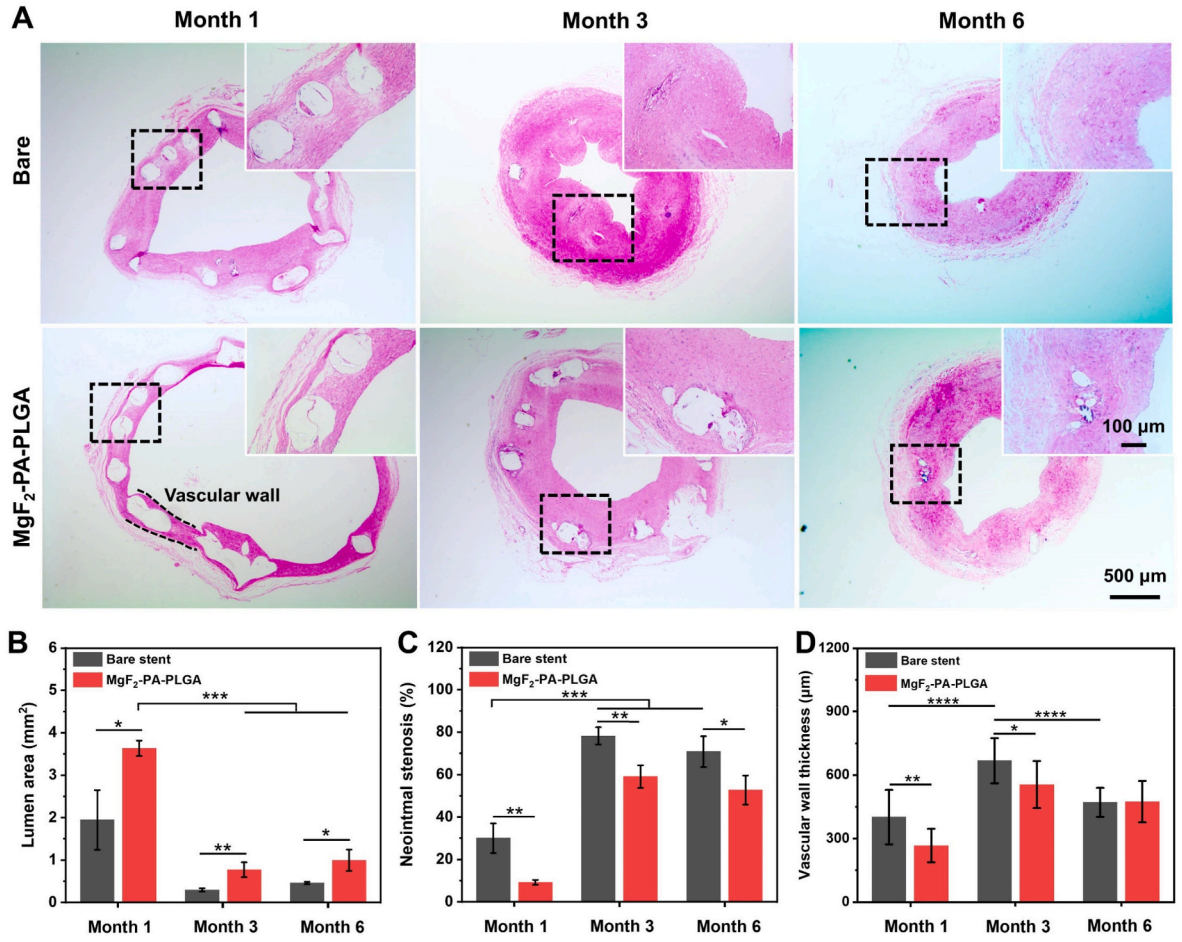

Fig. 11. (A) Hematoxylin-eosin (H&E) staining images of iliac artery sections after 1, 3, and 6 months of implantation of MgF_2-PA-PLGA and bare ZM21 stents. Vascular restenosis rate (B), lumen area (C), and vascular wall thickness (D) were calculated by Image J software. Data are presented as mean ± SD (n = 4), *p < 0.05, **p < 0.01, ***p < 0.001, ****p < 0.0001.

demonstrated for PA coatings sprayed with PTMC and APTES, they are attributed to the synergistic functions of APTES and PTMC performance. In addition, spraying PLGA over the PA coating overcomes the peeling issue caused by the inadequate adhesion between the polymer and the Mg substrate [61]. Simultaneously, the PLGA top layer is not only corrosion resistant but may also be employed as a medication carrier. This will promote the synergistic function of various coatings.

In addition, an improved gas volume detection device with enough resolution was utilized. *In vitro* evaluation results showed that the corrosion resistance of the MgF_2-PA-PLGA-coated stent was significantly improved compared with the bare stent. Although the MgF_2-PA-PLGA-coated stents had excellent corrosion resistance in static immersion, similar to all other stents, the SEM images of the stents after corrosion revealed that the corrosion degree of the stent bending sections was much higher than that of other parts. It has been demonstrated that during stent compression and expansion, stress concentrations are observed at stent bending locations [67]. Although the degree of stress concentration can still be reduced by optimizing the structure [3,65], it remains inevitable. Therefore, the coating's protection just delays the beginning of corrosion in the stress concentration area [68]. Fig. 12 depicts the stent's coating state alterations during expansion and immersion, as determined by comparing the corrosion morphology *in vitro* and *in vivo*. After spraying, the stent surface showed a homogeneous and dense coating. Nevertheless, when the stent is compressed and expanded, the coating on the inner surface is subjected to tensile stress due to the stent's plastic deformation. On the one hand, the coating of the deformed portion gets thinner under the influence of tensile tension. In addition, under the effect of the corrosion medium, the coating at tensile stress is more likely to be eroded and generate defects or cracks [37,69], and the formation of defects or cracks increases the corrosion rate and corrosion non-uniformity [70].

Establishing the connection between *in vivo* and *in vitro* is an urgent task to be solved at present [71]. It is widely accepted that *in vitro* corrosion is more severe than *in vivo* corrosion, as indicated by prior

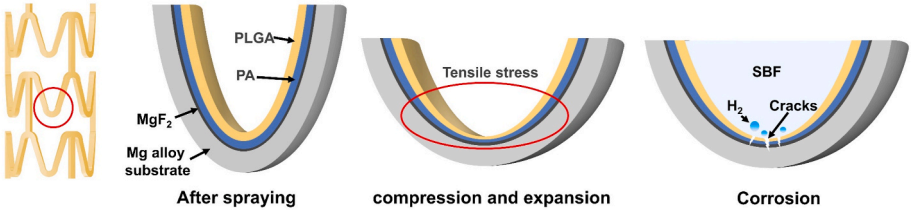

Fig. 12. Schematic depicting the change of the stent's coating during expansion and the corrosion process during immersion.

research [72,73]. The Micro-CT results of the stent implanted for one month revealed that the MgF_2-PA-PLGA coated stent still had its complete physical structure and provided enough radial support for the blood vessel. However, there were traces of corrosion in a few stress concentration regions, which was consistent with the *in vitro* corrosion results. The stent's mass loss rate reached 50% three months after implantation, with localized corrosion predominating. As depicted in Figs. S4–A, the mass loss of *in vitro* immersion for 14 and 21 days was 23.7 ± 8.3% and 80.3 ± 25%, respectively. It is clear that the corrosion accelerated during the 14–20 days of immersion. The coating degradation and the increase of the defect area are the primary causes of the stent's rapid corrosion. The degradation rates were 17.4 ± 3.4% and 50.5 ± 10.55% after 1 and 3 months of implantation *in vivo*, respectively (Figs. S4–B). In contrast to the *in vitro* degradation process, the *in vivo* degradation process exhibits no obvious corrosion acceleration. The impact of coating degradation and endothelialization on the material's corrosion rate should also be considered. Endothelialization of the stent after implantation *in vivo* slows corrosion, but the consistently high ion exchange rate between the stent and the electrolyte during the corrosion process *in vitro* promotes coating degradation and corrosion of the stent. As shown in Figs. S4–C, the corrosion rate ratios of 14 days *in vitro* to 30 days and 90 days *in vivo* were 2.91 ± 0.59 and 3.02 ± 1.2, and the corrosion rate ratios of 21 days *in vitro* to 30 days and 90 days *in vivo* were 6.86 ± 1.17 and 6.63 ± 1.15, respectively. Studies have also shown that for samples with <20% corrosion, an approximate *in vitro-in vivo* multiple of 1.3 ± 0.2 is used, while when Mg samples are degraded by 25–35%, a multiplier of 1.8 ± 0.2 becomes appropriate [74]. Comparing *in vitro* and *in vivo* mechanical behavior during degradation, the combined *in vitro* and *in vivo* metric value was 3.1 ± 0.7 [71]. It is clear that any approximate multiples of *in vivo* and *in vitro* can only be compared under certain evaluation conditions. Outside of assessment conditions, evaluating the relationship between *in vivo* and *in vitro* would be meaningless.

For BRS, it is required that the degradation products of the stents do not cause local or systemic toxicity and are expected to contribute to the remodeling and healing process of blood vessels [75,76]. This not only necessitates that the materials of the stent be biocompatible but also assures that the stents be capable of promoting endothelialization and offering adequate mechanical support *in vivo*. Rapid endothelialization has been demonstrated to be crucial for inhibiting intimal hyperplasia, restenosis, and late stent thrombosis [77,78]. An ideal biodegradable stent is considered to be able to strike a balance between degradation and mechanical integrity after implantation [79]. Theoretically, the stent should provide sufficient mechanical support for the first six months, while gradually degrading and remodeling the vessel over the next 6–12 months [79,80]. After this period, the presence of the stent *in vivo* has no positive impact [2,81]. It has also been recently reported that degradable stents should maintain radial support of the vessel for 3–4 months to aid in vascular remodeling [82].

Although the micro-CT data indicated that the effective support time of the stent was less than 3 months, the findings of biocompatibility research are really encouraging. The scanning electron microscope and laser confocal pictures in Fig. 10 indicate that the stent quickly endothelialized one month after implantation and that the vessel began remodeling at six months as the stent degraded. The HE staining data in Fig. 11 also showed that the bare stent was substantially degraded at 3 months with severe intimal hyperplasia, but this phenomenon was significantly improved at 6 months, and no corrosion product residue was observed. At 3 months, intimal hyperplasia is primarily caused by fast stent degradation that results in "overload" of degradation products and vascular rebound from the lack of support force [3,83]. Additionally, studies have shown that low Mg^{2+} concentrations (10 mM) increas cell survival, proliferation rate, and cell adhesion. Higher concentrations of Mg^{2+} (40–60 mM) exhibited the opposite impact on cells [84]. After six months, the degrading microenvironment shifted due to the dissolved remnants of the stent, and the vessels were rebuilt. For MgF_2-PA-PLGA-coated stents, the degree of intimal hyperplasia was much lower than that of bare stents, which was related to the slow degradation of stents [3,85]. Although the *in vitro* evaluation demonstrated that the MgF_2-PA-PLGA stents were non-cytotoxic, the extract could not truly reflect the microenvironment after stent degradation. Fig. 3D shows that there is a low level of Mg^{2+} release early in the immersion, but corrosion acceleration occurs later in the immersion and the concentration of Mg^{2+} increases significantly. Even though degradation is different *in vivo* and *in vitro*, the continued degradation of the stent after endothelialization also causes a rise in the local pH and the concentration of Mg^{2+}. This may be the primary cause of intimal hyperplasia. The gradual disappearance of corrosion products proved that the stent was completely absorbed *in vivo*. This eliminates concerns regarding the implant's long-term safety due to prolonged degradation. It should be noted that although the results in Fig. 11C showed that the lumen area was significantly reduced after three months, the reduction in radial support force due to stent degradation was still not negligible [86], which led to the contraction of isolated vessels when there was no blood pressure.

The above study revealed that surface-modified ZM21 stents exhibited superior corrosion control effects and biocompatibility compared to bare ZM21 stents. Although the performance of the stents in this study was significantly improved, there are still several flaws: (1) The degradation correlation between *in vitro* and long-term *in vivo* implants is unclear. (2) Although it has been shown that stress concentration has negative effects on coatings, this issue is not entirely resolved. (3) The durability of stents still does not meet the requirements, and the surface modification coating technology still needs to be improved. These works will be covered in a further study.

5. Conclusions

In summary, we developed a "built-up" composite film fabrication technique to improve the corrosion control effects of Mg alloy BRS. The degradation mechanism of MgF_2-PA-PLGA-coated stents was determined by corrosion *in vitro* and stent implantation *in vivo*. The results showed that the MgF_2-PA-PLGA coated stents still had mechanical integrity one month after implantation compared to bare ZM21 stents. The mass loss was 50.49 ± 10.6% at three months of implantation and almost complete at six months. The stress concentration induced during stent compression and expansion is the main factor leading to the early degradation of MgF_2-PA-PLGA-coated stents. Although rapid degradation led to intimal hyperplasia three months after the MgF_2-PA-PLGA-coated stent was implanted, the level of intimal hyperplasia was greatly reduced at 6 months after implantation, and no foreign matter remained in the tissue, suggesting full resorption of the ZM21 stent with its coating. Therefore, we believe that although rare earth-free Mg alloys have faster corrosion rates, they still have great potential in the field of BRS as long as their degradation rates can be reasonably controlled through coating modification.

Ethics approval and consent to participate

All stent implantation procedures complied with the Guide for the Care and Use of Laboratory Animals and the Regulations on the Administration of Laboratory Animals of Southwest Jiaotong University.

CRediT authorship contribution statement

Zhenglong Dou: Conceptualization, Methodology, Investigation, Formal analysis, Data curation, Writing – original draft. **Shuiling Chen:** Data curation, Methodology, Investigation. **Jiacheng Wang:** Methodology, Investigation. **Li Xia:** Methodology, Investigation. **Manfred F. Maitz:** Writing – review & editing. **Qiufen Tu:** Methodology, Resources. **Wentai Zhang:** Writing – review & editing. **Zhilu Yang:** Project administration, Funding acquisition, Writing – review & editing. **Nan**

Huang: Methodology, Funding acquisition, Project administration, Supervision, Writing – review & editing.

Declaration of competing interest

The authors declare that they have no known competing financial interests or personal relationships that could have appeared to influence the work reported in this paper.

Acknowledgements

This work was supported by the National Natural Science Foundation of China (Project 32171326, 82072072, 81330031), the INTERNATIONAL COOPERATION Project by Science and Technology Department of Sichuan Province (2021YslnFH0056), and the High-level Talents Research and Development Program of Affiliated Dongguan Hospital (K202102).

Appendix A. Supplementary data

Supplementary data to this article can be found online at https://doi.org/10.1016/j.bioactmat.2023.02.004.

References

[1] H. Chen, W. Yang, H. Chen, L. Liu, F. Gao, X. Yang, Q. Jiang, Q. Zhang, Y. Wang, Surface modification of mitoxantrone-loaded PLGA nanospheres with chitosan, Colloids Surf. B Biointerfaces 73 (2) (2009) 212–218.
[2] M. Moravej, D. Mantovani, Biodegradable metals for cardiovascular stent application: interests and new opportunities, Int. J. Mol. Sci. 12 (7) (2011) 4250–4270.
[3] B. Heublein, R. Rohde, V. Kaese, M. Niemeyer, W. Hartung, A. Haverich, Biocorrosion of magnesium alloys: a new principle in cardiovascular implant technology? Heart 89 (6) (2003) 651–656.
[4] W. Ding, Opportunities and challenges for the biodegradable magnesium alloys as next-generation biomaterials, Regener. biomater. 3 (2) (2016) 79–86.
[5] W. Wu, S. Chen, D. Gastaldi, L. Petrini, D. Mantovani, K. Yang, L. Tan, F. Migliavacca, Experimental data confirm numerical modeling of the degradation process of magnesium alloys stents, Acta Biomater. 9 (10) (2013) 8730–8739.
[6] G. Song, Control of biodegradation of biocompatable magnesium alloys, Corrosion Sci. 49 (4) (2007) 1696–1701.
[7] X. Wang, D. Xu, R. Wu, X. Chen, Q. Peng, L. Jin, Y. Xin, Z. Zhang, Y. Liu, X. Chen, What is going on in magnesium alloys? J. Mater. Sci. Technol. 34 (2) (2018) 245–247.
[8] G.L. Song, A. Atrens, Corrosion mechanisms of magnesium alloys, Adv. Eng. Mater. 1 (1) (1999) 11–33.
[9] G. Song, A. Atrens, Understanding magnesium corrosion—a framework for improved alloy performance, Adv. Eng. Mater. 5 (12) (2003) 837–858.
[10] Y. Ding, C. Wen, P. Hodgson, Y. Li, Effects of alloying elements on the corrosion behavior and biocompatibility of biodegradable magnesium alloys: a review, J. Mater. Chem. B 2 (14) (2014) 1912–1933.
[11] J. Walker, S. Shadanbaz, T.B. Woodfield, M.P. Staiger, G.J. Dias, Magnesium biomaterials for orthopedic application: a review from a biological perspective, J. Biomed. Mater. Res. B Appl. Biomater. 102 (6) (2014) 1316–1331.
[12] Y. Su, J. Fu, S. Du, E. Georgas, Y.-X. Qin, Y. Zheng, Y. Wang, D. Zhu, Biodegradable Zn–Sr alloys with enhanced mechanical and biocompatibility for biomedical applications, Smart Mater. Med. 3 (2022) 117–127.
[13] S. Agarwal, J. Curtin, B. Duffy, S. Jaiswal, Biodegradable magnesium alloys for orthopaedic applications: a review on corrosion, biocompatibility and surface modifications, Mater. Sci. Eng. C 68 (2016) 948–963.
[14] W. Liu, F. Cao, L. Chang, Z. Zhang, J. Zhang, Effect of rare earth element Ce and La on corrosion behavior of AM60 magnesium alloy, Corrosion Sci. 51 (6) (2009) 1334–1343.
[15] S. Hirano, K.T. Suzuki, Exposure, metabolism, and toxicity of rare earths and related compounds, Environ. Health Perspect. 104 (suppl 1) (1996) 85–95.
[16] F. Feyerabend, J. Fischer, J. Holtz, F. Witte, R. Willumeit, H. Drücker, C. Vogt, N. Hort, Evaluation of short-term effects of rare earth and other elements used in magnesium alloys on primary cells and cell lines, Acta Biomater. 6 (5) (2010) 1834–1842.
[17] D.-s. Yin, E.-l. Zhang, S.-y. Zeng, Effect of Zn on mechanical property and corrosion property of extruded Mg-Zn-Mn alloy, Trans. Nonferrous Metals Soc. China 18 (4) (2008) 763–768.
[18] O. Lunder, T.K. Aune, K. Nisancioglu, Effect of Mn additions on the corrosion behavior of mould-cast magnesium ASTM AZ91, Corrosion 43 (5) (1987) 291–295.
[19] G. Makar, J. Kruger, Corrosion of magnesium, Int. Mater. Rev. 38 (3) (1993) 138–153.
[20] Y. Tang, L. Zhu, P. Zhang, K. Zhao, Z. Wu, Enhanced corrosion resistance of bio-piezoelectric composite coatings on medical magnesium alloys, Corrosion Sci. 176 (2020), 108939.
[21] J. Yang, F. Cui, I.S. Lee, Surface modifications of magnesium alloys for biomedical applications, Ann. Biomed. Eng. 39 (7) (2011) 1857–1871.
[22] T.S. Narayanan, I.-S. Park, M.-H. Lee, Surface Modification of Magnesium and its Alloys for Biomedical Applications: Opportunities and Challenges, Surface Modification of Magnesium and its Alloys for Biomedical Applications, 2015, pp. 29–87.
[23] X. Li, X. Liu, S. Wu, K. Yeung, Y. Zheng, P.K. Chu, Design of magnesium alloys with controllable degradation for biomedical implants: from bulk to surface, Acta Biomater. 45 (2016) 2–30.
[24] P. Tong, Y. Sheng, R. Hou, M. Iqbal, L. Chen, J. Li, Recent progress on coatings of biomedical magnesium alloy, Smart Mater. Med. (2021) 104–116.
[25] Z.-Z. Yin, W.-C. Qi, R.-C. Zeng, X.-B. Chen, C.-D. Gu, S.-K. Guan, Y.-F. Zheng, Advances in coatings on biodegradable magnesium alloys, J. Magn. Alloys 8 (1) (2020) 42–65.
[26] J. Wang, J. Tang, P. Zhang, Y. Li, J. Wang, Y. Lai, L. Qin, Surface modification of magnesium alloys developed for bioabsorbable orthopedic implants: a general review, J. Biomed. Mater. Res. B Appl. Biomater. 100 (6) (2012) 1691–1701.
[27] H.-y. Li, D.-n. Huang, K.-f. Ren, J. Ji, Inorganic-polymer composite coatings for biomedical devices, Smart Mater. Med. 2 (2021) 1–14.
[28] N. Li, Y. Li, Y. Wang, M. Li, Y. Cheng, Y. Wu, Y. Zheng, Corrosion resistance and cytotoxicity of a MgF2 coating on biomedical Mg–1Ca alloy via vacuum evaporation deposition method, Surf. Interface Anal. 45 (8) (2013) 1217–1222.
[29] D. Dvorsky, J. Kubasek, E. Jablonska, J. Kaufmanova, D. Vojtech, Mechanical, corrosion and biological properties of advanced biodegradable Mg–MgF2 and WE43-MgF2 composite materials prepared by spark plasma sintering, J. Alloys Compd. 825 (2020), 154016.
[30] J. Li, S. Wang, Y. Sheng, C. Liu, Z. Xue, P. Tong, S. Guan, Designing HA/PEI nanoparticle composite coating on biodegradable Mg–Zn–Y-Nd alloy to direct cardiovascular cells fate, Smart Mater. Med. 2 (2021) 124–133.
[31] J.-H. Jo, B.-G. Kang, K.-S. Shin, H.-E. Kim, B.-D. Hahn, D.-S. Park, Y.-H. Koh, Hydroxyapatite coating on magnesium with MgF2 interlayer for enhanced corrosion resistance and biocompatibility, J. Mater. Sci. Mater. Med. 22 (11) (2011) 2437–2447.
[32] Y. Chen, Y. Song, S. Zhang, J. Li, C. Zhao, X. Zhang, Interaction between a high purity magnesium surface and PCL and PLA coatings during dynamic degradation, Biomed. Mater. 6 (2) (2011), 025005.
[33] L.-Y. Li, L.-Y. Cui, R.-C. Zeng, S.-Q. Li, X.-B. Chen, Y. Zheng, M.B. Kannan, Advances in functionalized polymer coatings on biodegradable magnesium alloys–A review, Acta Biomater. 79 (2018) 23–36.
[34] P. Shi, B. Niu, E. Shanshan, Y. Chen, Q. Li, Preparation and characterization of PLA coating and PLA/MAO composite coatings on AZ31 magnesium alloy for improvement of corrosion resistance, Surf. Coating. Technol. 262 (2015) 26–32.
[35] W. Zhang, Y. Chen, M. Chen, S. Zhao, J. Mao, A. Qu, W. Li, Y. Zhao, N. Huang, G. Wan, Strengthened corrosion control of poly (lactic acid)(PLA) and poly (ε-caprolactone)(PCL) polymer-coated magnesium by imbedded hydrophobic stearic acid (SA) thin layer, Corrosion Sci. 112 (2016) 327–337.
[36] J. Liu, T. Xi, Enhanced anti-corrosion ability and biocompatibility of PLGA coatings on MgZnYNd alloy by BTSE-APTES pre-treatment for cardiovascular stent, J. Mater. Sci. Technol. 32 (9) (2016) 845–857.
[37] L. Chen, Y. Sheng, H. Zhou, Z. Li, X. Wang, W. Li, Influence of a MAO+ PLGA coating on biocorrosion and stress corrosion cracking behavior of a magnesium alloy in a physiological environment, Corrosion Sci. 148 (2019) 134–143.
[38] J. Wang, Y. He, M.F. Maitz, B. Collins, K. Xiong, L. Guo, Y. Yun, G. Wan, N. Huang, A surface-eroding poly (1, 3-trimethylene carbonate) coating for fully biodegradable magnesium-based stent applications: toward better biofunction, biodegradation and biocompatibility, Acta Biomater. 9 (10) (2013) 8678–8689.
[39] H. Tang, S. Li, Y. Zhao, C. Liu, X. Gu, Y. Fan, A surface-eroding poly (1, 3-trimethylene carbonate) coating for magnesium based cardiovascular stents with stable drug release and improved corrosion resistance, Bioact. Mater. 7 (2022) 144–153.
[40] M. Taylor, A. Daniels, K. Andriano, J. Heller, Six bioabsorbable polymers: in vitro acute toxicity of accumulated degradation products, J. Appl. Biomater. 5 (2) (1994) 151–157.
[41] A. Campbell, The potential role of aluminium in Alzheimer's disease, Nephrol. Dial. Transplant. 17 (suppl_2) (2002) 17–20.
[42] H.K. Makadia, S.J. Siegel, Poly lactic-co-glycolic acid (PLGA) as biodegradable controlled drug delivery carrier, Polymers 3 (3) (2011) 1377–1397.
[43] J. Li, P. Cao, X. Zhang, S. Zhang, Y. He, In vitro degradation and cell attachment of a PLGA coated biodegradable Mg–6Zn based alloy, J. Mater. Sci. 45 (22) (2010) 6038–6045.
[44] X. Wang, S.S. Venkatraman, F.Y. Boey, J.S. Loo, L.P. Tan, Controlled release of sirolimus from a multilayered PLGA stent matrix, Biomaterials 27 (32) (2006) 5588–5595.
[45] X. Zhu, R.D. Braatz, A mechanistic model for drug release in PLGA biodegradable stent coatings coupled with polymer degradation and erosion, J. Biomed. Mater. Res. 103 (7) (2015) 2269–2279.
[46] C.L. Huang, S. Kumar, J.J. Tan, F.Y. Boey, S.S. Venkatraman, T.W. Steele, J.S. Loo, Modulating drug release from poly (lactic-co-glycolic acid) thin films through terminal end-groups and molecular weight, Polym. Degrad. Stabil. 98 (2) (2013) 619–626.
[47] A.F. 18a, Standard Guide for in Vitro Degradation Testing of Absorbable Metals1, ASTM International, West Conshohocken, PA, USA, 2018.

[48] C. Wang, H. Fang, C. Hang, Y. Sun, Z. Peng, W. Wei, Y. Wang, Fabrication and characterization of silk fibroin coating on APTES pretreated Mg-Zn-Ca alloy, Mater. Sci. Eng. C 110 (2020), 110742.
[49] M. Pagliaro, Silica-based Materials for Advanced Chemical Applications, Royal Society of Chemistry, 2009.
[50] T. Kokubo, H. Takadama, How useful is SBF in predicting in vivo bone bioactivity? Biomaterials 27 (15) (2006) 2907–2915.
[51] A. Nace, Standard Guide for Laboratory Immersion Corrosion Testing of Metals, ASTM Int., 2012, pp. 1–9.
[52] I. Standard, Biological Evaluation of Medical Devices—Part 5: Tests for in Vitro Cytotoxicity, International Organization for Standardization, Geneve, Switzerland, 2009.
[53] J.-T. Han, S.-Y. Lee, Y.-H. Lee, N.-I. Baek, Antioxidative diarylheptanoids from the fruits of Alpinia oxyphylla, Food Sci. Biotechnol. 16 (6) (2007) 1060–1063.
[54] Y. Yang, X. Li, H. Qiu, P. Li, P. Qi, M.F. Maitz, T. You, R. Shen, Z. Yang, W. Tian, Polydopamine modified TiO2 nanotube arrays for long-term controlled elution of bivalirudin and improved hemocompatibility, ACS Appl. Mater. Interfaces 10 (9) (2017) 7649–7660.
[55] H. Hornberger, S. Virtanen, A.R. Boccaccini, Biomedical coatings on magnesium alloys–a review, Acta Biomater. 8 (7) (2012) 2442–2455.
[56] R.-G. Hu, S. Zhang, J.-F. Bu, C.-J. Lin, G.-L. Song, Recent progress in corrosion protection of magnesium alloys by organic coatings, Prog. Org. Coating 73 (2–3) (2012) 129–141.
[57] T. Yan, L. Tan, B. Zhang, K. Yang, Fluoride conversion coating on biodegradable AZ31B magnesium alloy, J. Mater. Sci. Technol. 30 (7) (2014) 666–674.
[58] X. Liu, Z. Yue, T. Romeo, J. Weber, T. Scheuermann, S. Moulton, G. Wallace, Biofunctionalized anti-corrosive silane coatings for magnesium alloys, Acta Biomater. 9 (10) (2013) 8671–8677.
[59] J. Song, W. Van Ooij, Bonding and corrosion protection mechanisms of γ-APS and BTSE silane films on aluminum substrates, J. Adhes. Sci. Technol. 17 (16) (2003) 2191–2221.
[60] J. Liu, B. Zheng, P. Wang, X. Wang, B. Zhang, Q. Shi, T. Xi, M. Chen, S. Guan, Enhanced in vitro and in vivo performance of Mg–Zn–Y–Nd alloy achieved with APTES pretreatment for drug-eluting vascular stent application, ACS Appl. Mater. Interfaces 8 (28) (2016) 17842–17858.
[61] M.-H. Kang, K.-H. Cheon, K.-I. Jo, J.-H. Ahn, H.-E. Kim, H.-D. Jung, T.-S. Jang, An asymmetric surface coating strategy for improved corrosion resistance and vascular compatibility of magnesium alloy stents, Mater. Des. 196 (2020), 109182.
[62] N. Winzer, A. Atrens, G. Song, E. Ghali, W. Dietzel, K.U. Kainer, N. Hort, C. Blawert, A critical review of the stress corrosion cracking (SCC) of magnesium alloys, Adv. Eng. Mater. 7 (8) (2005) 659–693.
[63] M. Abdalla, A. Joplin, M. Elahinia, H. Ibrahim, Corrosion modeling of magnesium and its alloys for biomedical applications, Corrosion and Materials Degradation 1 (2) (2020) 11.
[64] P.D. Stein, H.N. Sabbah, Measured turbulence and its effect on thrombus formation, Circ. Res. 35 (4) (1974) 608–614.
[65] D. Bian, X. Zhou, J. Liu, W. Li, D. Shen, Y. Zheng, W. Gu, J. Jiang, M. Li, X. Chu, Degradation behaviors and in-vivo biocompatibility of a rare earth-and aluminum-free magnesium-based stent, Acta Biomater. 124 (2021) 382–397.
[66] T. Kraus, S.F. Fischerauer, A.C. Hänzi, P.J. Uggowitzer, J.F. Löffler, A.M. Weinberg, Magnesium alloys for temporary implants in osteosynthesis: in vivo studies of their degradation and interaction with bone, Acta Biomater. 8 (3) (2012) 1230–1238.
[67] C. Chen, J. Chen, W. Wu, Y. Shi, L. Jin, L. Petrini, L. Shen, G. Yuan, W. Ding, J. Ge, In vivo and in vitro evaluation of a biodegradable magnesium vascular stent designed by shape optimization strategy, Biomaterials 221 (2019), 119414.
[68] J.E. Gray-Munro, C. Seguin, M. Strong, Influence of surface modification on the in vitro corrosion rate of magnesium alloy AZ31, journal of biomedical materials research Part A: an official journal of the society for biomaterials, The Japanese Society for Biomaterials, and The Australian Society for Biomaterials and the Korean Society for Biomaterials 91 (1) (2009) 221–230.
[69] P.B. Srinivasan, C. Blawert, W. Dietzel, K. Kainer, Stress corrosion cracking behaviour of a surface-modified magnesium alloy, Scripta Mater. 59 (1) (2008) 43–46.
[70] A. Tan, A. Soutar, I. Annergren, Y. Liu, Multilayer sol–gel coatings for corrosion protection of magnesium, Surf. Coating. Technol. 198 (1–3) (2005) 478–482.
[71] P.K. Bowen, J. Drelich, J. Goldman, A new in vitro–in vivo correlation for bioabsorbable magnesium stents from mechanical behavior, Mater. Sci. Eng. C 33 (8) (2013) 5064–5070.
[72] F. Witte, J. Fischer, J. Nellesen, H.-A. Crostack, V. Kaese, A. Pisch, F. Beckmann, H. Windhagen, In vitro and in vivo corrosion measurements of magnesium alloys, Biomaterials 27 (7) (2006) 1013–1018.
[73] J. Wang, L. Liu, Y. Wu, M.F. Maitz, Z. Wang, Y. Koo, A. Zhao, J. Sankar, D. Kong, N. Huang, Ex vivo blood vessel bioreactor for analysis of the biodegradation of magnesium stent models with and without vessel wall integration, Acta Biomater. 50 (2017) 546–555.
[74] P.K. Bowen, A. Drelich, J. Drelich, J. Goldman, Rates of in vivo (arterial) and in vitro biocorrosion for pure magnesium, J. Biomed. Mater. Res. 103 (1) (2015) 341–349.
[75] H. Yang, C. Wang, C. Liu, H. Chen, Y. Wu, J. Han, Z. Jia, W. Lin, D. Zhang, W. Li, Evolution of the degradation mechanism of pure zinc stent in the one-year study of rabbit abdominal aorta model, Biomaterials 145 (2017) 92–105.
[76] Y.-c. Hou, F. Witte, J. Li, S. Guan, The increased ratio of Mg2+/Ca2+ from degrading magnesium alloys directs macrophage fate for functionalized growth of endothelial cells, Smart Mater. Med. 3 (2022) 188–198.
[77] Y. Yang, P. Gao, J. Wang, Q. Tu, L. Bai, K. Xiong, H. Qiu, X. Zhao, M.F. Maitz, H. Wang, Endothelium-mimicking multifunctional coating modified cardiovascular stents via a stepwise metal-catechol-(amine) surface engineering strategy, Research 2020 (2020), 9203906.
[78] J. Wang, Y. Xue, J. Liu, M. Hu, H. Zhang, K. Ren, Y. Wang, J. Ji, Hierarchical capillary coating to biofunctionlize drug-eluting stent for improving endothelium regeneration, Research 2020 (2020) 1458090.
[79] H. Hermawan, D. Dubé, D. Mantovani, Developments in metallic biodegradable stents, Acta Biomater. 6 (5) (2010) 1693–1697.
[80] A. Schömig, A. Kastrati, H. Mudra, R. Blasini, H. Schühlen, V. Klauss, G. Richardt, F.J. Neumann, Four-year experience with Palmaz-Schatz stenting in coronary angioplasty complicated by dissection with threatened or present vessel closure, Circulation 90 (6) (1994) 2716–2724.
[81] M. Heiden, E. Walker, L. Stanciu, Magnesium, iron and zinc alloys, the trifecta of bioresorbable orthopaedic and vascular implantation-a review, J. Biotechnol. Biomater. 5 (2) (2015) 1.
[82] Y.F. Zheng, X.N. Gu, F. Witte, Biodegradable metals, Mater. Sci. Eng. R Rep. 77 (2014) 1–34.
[83] Y. Yue, L. Wang, N. Yang, J. Huang, L. Lei, H. Ye, L. Ren, S. Yang, Effectiveness of biodegradable magnesium alloy stents in coronary artery and femoral artery, J. Intervent. Cardiol. 28 (4) (2015) 358–364.
[84] J. Ma, N. Zhao, D. Zhu, Biphasic responses of human vascular smooth muscle cells to magnesium ion, J. Biomed. Mater. Res., Part A 104 (2) (2016) 347–356.
[85] R. Waksman, R. Erbel, C. Di Mario, J. Bartunek, B. de Bruyne, F.R. Eberli, P. Erne, M. Haude, M. Horrigan, C. Ilsley, Early-and long-term intravascular ultrasound and angiographic findings after bioabsorbable magnesium stent implantation in human coronary arteries, JACC Cardiovasc. Interv. 2 (4) (2009) 312–320.
[86] J. Zhang, H. Li, W. Wang, H. Huang, J. Pei, H. Qu, G. Yuan, Y. Li, The degradation and transport mechanism of a Mg-Nd-Zn-Zr stent in rabbit common carotid artery: a 20-month study, Acta Biomater. 69 (2018) 372–384.